GSK-3 regulates CD4-CD8 cooperation needed to generate super-armed CD8+ cytolytic T cells against tumors

Bastien Moës[1-3], Janna Krueger[1-3], Alexandra Kazanova[1-3], Chen Liu[1-3], Yunfeng Gao[1-3], Nikhil Anto Ponnoor[1-3], Linda Castoun-Puckett[1-3], Andres Carlos Oroya Lazo[1-3], Lan Huong[1-3], Auryane Laure Cabald[1-3], Thai Hien Tu[1-3] and Christopher E. Rudd[1-5*]

1. Department of Medicine and Sciences biomédicales, Université de Montréal, Montréal, QC H3C 3J7, Canada
2. Dept de microbiologie, infectiologie et immunologie, Université de Montréal
3. Cell Signaling and Immunotherapy Section, Research Center Hopital Maisonneuve-Rosemont (CR-HMR) Montreal, Quebec H1T 2M4
4. Department of Medicine, McGill University
5. University Institute for Hematology-Oncology and Cell Therapy, Hopital Maisonneuve-Rosemont, Montreal, QC H1T 2M4, Canada

* Corresponding Author**:** Christopher E. Rudd, CR-HMR, University of Montreal, 5345 Assomption boulevard, H1T 2M4, Montréal, Québec, Canada, Phone: 1-514- 252 3400, Email adress : christopher.e.rudd@umontreal.ca

Authors contribution :

Conception and design: B.M., J.K. and C.E.R.

Development of methodology: B.M., J.K and A.K.

Acquisition of data: B.M., J.K, A.K., C.L, Y.G., N.A.P., L.C.P., L.H, A.L.C. and H.T.

Analysis and interpretation of data: B.M., J.K and A.K.

Writing, review, and/or revision of the manuscript: B.M. and C.E.R.

Administrative, technical, or material support: B.M., J.K, A.K. and C.E.R

Study supervision: B.M. and C.E.R.

Competing Interests Statement: C.E.R has received consulting fees from Freshfields Bruckhaus Deringer LLP (UK), Bristows LLP (UK), Proskaueh Rose LLP (US) for patent consultancy work and is the founder of ImmunAb Res Inc (Canada) with patents relating to immunotherapies. The other authors declare no competing interests.

Running Title: GSK3 controls CD4-CD8 cooperation and synergy with anti-PD-1

Abstract

While immune checkpoint blockade (ICB) has revolutionized cancer treatment, the key T-cell signaling pathways responsible for its potency remain unclear. GSK-3 is an inhibitory kinase that is most active in resting T-cells. In this study, we demonstrate that GSK-3 facilitates PD-1 blockade, an effect seen by modulating CD4 T-cell help for CD8+ CTL responses against ICB resistant tumors. We show that GSK-3 controls metabolic reprogramming towards glycolysis and synergizes with PD-1 to induce a transcriptional program that reduces suppressive CD4+ Treg numbers while generating super-armed effector-memory CD8+ CTLs that express an unprecedented 7/9 granzymes from the genome. Crucially, we found that GSK-3 cooperates with PD-1 blockade to determine the dependency of CD8+ CTLs on help from CD4+ T-cells. Our study unravels a novel cooperative PD-1 blockade-dependent signaling pathway that potentiates CTL responses against tumors, offering a new strategy to overcome immunotherapy resistance by modulating CD4+ helper and CD8+ cytotoxic functions.

Significance

This study demonstrates for the first time that GSK-3 controls the crosstalk between CD4+ and CD8+ T cells, synergizing with anti-PD-1 therapy to overcome resistance to checkpoint blockade and to generate super-armed CD8+ effector cells in cancer immunotherapy. This newly uncovered GSK-3-dependent CD4-CD8 T-cell crosstalk mechanism presents a new approach to enhance anti-PD-1 immunotherapy.

Introduction

Antigen presenting cells, helper, suppressor T-cells as well as memory and effector subsets orchestrate the nature and amplitude of the adaptive immune response(1). CD4+ and CD8+ T-cells work together to eliminate virally infected cells as well as cancer (2, 3). CD4+ T-cells provide essential help for the development of long-lasting memory and cytotoxic effector CD8 cells (4-6). Without this support, CD8+ T-cell function is suboptimal, impairing their ability to control infections and tumor growth (4, 5, 7, 8). CD4 help can be through various mechanisms that include the production of cytokines such as IL-2, IFN-γ, and TNF-α, and by enhancing dendritic cell function (6). By contrast, CD4+FoxP3+ regulatory T-cells (Tregs) play a crucial role in maintaining immune tolerance while suppressing anti-tumor immune responses (9). The manipulation of CD4+ T-cell help versus Treg activity is a promising strategy for cancer immunotherapy (10, 11).

The continuous long-term exposure to antigens can also cause exhaustion which impairs the clearance of pathogens and tumors (12-14). While the transcription factor, T cell factor 1 (TCF-1) defines early progenitor and memory T cells (15-18), the expression of inhibitory co-receptors such as cytotoxic T-lymphocyte antigen 4 (CTLA-4), programmed death-1 (PD-1), and lymphocyte-activation gene 3 (LAG-3) limit T-cell responses(19). In this context, immune checkpoint blockade (ICB) has revolutionized cancer treatment (20-25). This is mediated by antibodies that block the signaling of inhibitory receptors, while also inducing internalisation (20-25). TCF-1+ T-cells are also essential for successful ICB (26-28), as is the development of effector cytolytic T-cells (CTLs) which release cytotoxic granules that contain perforin and granzymes (GZMs) needed to induce apoptosis in target cells (29, 30). Although granzyme B (GZMB) is the best studied GZM, 9 other GZMs are expressed in mice that act on overlapping and unique protein substrates (31, 32).

In addition, activation signals are needed to elicit the development of effective anti-tumor responses (33, 34) . These signals are mediated by protein-tyrosine, serine/threonine and lipid kinases as well as GTP binding proteins and downstream substrates (34-37). In this context, the protein-tyrosine kinase $p56^{lck}$, either free or associated with the CD4 or CD8 co-receptors initiates the activation cascade (33, 38, 39). The kinase phosphorylates T-cell receptor (TCR) associated CD3 and ζ chain immunoreceptor tyrosine-based activation motifs (ITAMs) (33, 38). This then leads to the recruitment of a second zeta-chain-associated protein kinase 70 (ZAP-70) (40). Together, these kinases phosphorylate and activate the function of downstream

enzymes and adaptor proteins that are needed to integrate signals for transcription factor entry into the nucleus and gene transcription (41).

Unlike $p56^{lck}$ and ZAP-70 which are activated by receptors on the surface of T-cells, glycogen synthase kinase-3 (GSK-3) is a serine/threonine kinase which is constitutively active in quiescent T-cells and becomes inhibited in response to receptor ligation (42, 43). In mammals, two isoforms of GSK-3 have been identified the 51 kDa GSK-3α isoform and a 47 kDa GSK-3β isoform which are encoded by separate genes (43). The phosphorylation of specific serine residues (Ser9: GSK-3β, Ser21: GSK-3α) inactivate the kinase (44, 45). By contrast, phosphorylation at Tyr216: GSK-3β, Tyr279: GSK-3α enhances activity (46, 47). Both isoforms are expressed in numerous tissues (48) and regulate diverse processes (46, 49). This includes the inhibition of glycogen synthase (50) regulation of β-catenin expression (51-53) as well as T-cell motility (54). In the context of tumor immunity, GSK-3 inactivation can downregulate PD-1 and LAG-3 transcription and expression (42, 55) and in the process, limit tumor growth (42, 54-59). In this regard, the FDA has approved studies using GSK-3 inhibitors to treat various cancers (60, 61).

While immune checkpoint blockade has revolutionized cancer treatment, the key T-cell signaling pathways responsible for its potency remain unclear. Further, the signaling mechanisms that are responsible for CD4-CD8 cooperation in checkpoint blockade therapy have remained elusive. Here, we show for the first time that GSK-3 controls CD4-CD8 T-cell cooperation which operates in synergy with anti-PD-1 to generate super-armed CD8+ effectors in immunotherapy. The genetic downregulation of GSK-3 promoted the presence of progenitor and memory CD8+ TILs while decreasing numbers of suppressor Treg TILs. Further, GSK-3 downregulation, combined with anti-PD-1, unlocked an unprecedented cytotoxic potential in CD8+ T-cells, enabling the expression of a 7 out of 9 granzymes from the mouse genome, a phenomenon not before observed. This uncovered GSK-3-regulated CD4-CD8 T-cell crosstalk mechanism could be exploited to enhance anti-PD-1 immunotherapy.

Results

GSK-3 KD mice show increased T-cell memory and less exhaustion in response to Cl 13 LCMV

123 To define further the role of GSK-3 in T-cell immunity, we first generated mice lacking
124 both GSK-3α and GSK-3β specifically in mature T cells. This was achieved by crossing distal
125 promoter lck-Cre mice (dlck-Cre) with mice carrying floxed alleles for gsk-3α (gsk-3αlox/lox)
126 and gsk-3β (gsk-3βlox/lox). The distal lck promoter drives Cre recombinase expression in
127 peripheral T cells, allowing for gene deletion specifically in mature T cells after their
128 development in the thymus (62). Immunoblotting with an anti-GSK-3α/β antibody showed a
129 >75% reduction in the expression of GSK-3α and GSK-3β in splenic T cells (**Fig. 1A**)
130 (referred to as GSK-3 knock-down (GSK-3KD) or dLCK-CRE).
131 We next assessed whether GSK-3 KD would affect responses to infection by chronic Cl
132 13 and acute Armstrong stains of LCMV, as described (42, 63). In the case of Cl13, the dLck-
133 CRE GSK-3 KD mice showed less weight loss from days 0-8 followed by a more rapid and
134 complete recovery from day 10-30, By contrast, wild type mice showed a more severe loss of
135 weight and a delayed recovery (**Fig. 1B**). Even by 30 days the weight of wild type mice had
136 not fully recovered to the level seen in dLck-CRE mice. By contrast, as a control, no
137 difference in the weight was observed following acute infection with LCMV Armstrong (**Fig.**
138 **1C**).
139 In terms of virally reactive cells, the spleens of GSK-3KD mice had higher levels of CD8+
140 T-cells than wild-type mice at day 30 in response to Cl13 and at day 7 in response to the
141 Armstrong strain (**Fig. 1D**). Among these cells, GSK-3KD mice showed greater numbers of
142 gp33 reactive effector memory (GP33+CD44+CD62L-) and central memory
143 (GP33+CD44+CD62L+) CD8+ T-cells in response to Cl13 as detected with tetramers
144 containing the GP33 peptide (**Fig. 1E**). Conversely, the numbers of GP33+ KLRG1+CD39+
145 terminal effector cells (TE) were reduced in GSK-3KD mice (**Fig. 1F**). This increased
146 generation of dLCK-CRE CD8 effector memory was also seen in response to the Armstrong
147 strain. Central memory cells were not detectable at this earlier 7-day time point (**Fig. 1G**).
148 These data demonstrate that reduced GSK-3 promotes the differentiation of CD8+ T-cells
149 into effector memory and central memory T-cells.
150 In terms of other subsets, we also observed increased numbers of CD4+ T-cells,
151 CD44+CD4+ T-cells, and CD44+Gp33+CD4+ T-cells in GSK-3KD mice relative to controls as
152 well as Th1, Th2 and FoxP3 Tregs (**Supplementary Figure S1**). In addition, we observed an
153 increase in total B cells, CD44+ B cells, and CD44+GP33+ B cells in GSK-3KD mice
154 compared to controls as well as germinal center CD44+ B-cell numbers in GSK-3KD mice
155 (**Supplementary Figure S2**).

156 Within these cells, GSK-3KD mice also showed an increase in the presence of the
157 progenitor CD8+ T-cell marker TCF1 (**Fig. 1H**). While the expression of TCF1 in the
158 CD8+CD44- population was lower in the GSK-3KD mice, the percent representation of
159 GP33+TCF1+ CD8+ T-cells within the CD44+ pool of experienced T-cells was routinely
160 higher in the GSK-3KD mice (**Fig. 1H**). This was observed in the overall CD8+GP33+
161 population as well as in the central and effector memory CD8+ compartments.
162 Consistent with these findings, GSK-3 KD mice gave rise to greater numbers of memory
163 precursor effector cells (MPECs) relative to short-lived effector cells (SLECs) when compared
164 to WT mice (**Fig. 1I**). MPECs were defined as KLRG1- IL7Rα+ while SLECs were defined as
165 KLRG1+IL7Rα-. A FACs plot of a representative experiment showed an increase in MPECs
166 (i.e., 27.1 to 39.2) in GSK-3 KD compared to WT mice. Conversely, there was a
167 corresponding decrease in SLECs. In a comparison of multiple mice, a similar effect was
168 observed where the numbers of GP33+CD8+ MPEC was higher in the GSK-3KD mice than
169 in the WT mice (**Fig. 1J**).
170 Interestingly, TCF1 was selectively expressed in the MPEC population, and this
171 expression was higher in the GSK-3KD CD8+ cells (**Fig. 1K**) and in a presentative FACs plot
172 of GP33+CD8+ T-cells from 33.6% in WT to 55.8% in GSK-3KD MPECs (**Fig. 1L**). Further,
173 importantly, cell division was only seen in the GP33+ MPEC population as shown by the
174 increase in the cell cycle marker Ki67 (**Fig. 1M,** upper panel). Ki67 is marker for cell
175 division(64) .The shorter lived SLECs also showed the presence of dividing cells but they
176 were similar in WT and KD mice (**Fig. 1M,** lower panel).
177 The reduction in GSK-3 also affected stages of CD8+ T-cell exhaustion. The stages
178 include progenitor PD-1+TCF-1+TIM3- cells which develop into transitionary cells (PD-
179 1+TIM-3+CX3CR1+) and finally into terminally exhausted (PD-1+TIM-3+CX3CR1-CD101+)
180 cells (65, 66). In this context, the expression of TIM-3 was significantly reduced in GSK-3 KD
181 GP33+ CD8+ T-cells (**Fig. 1N**). Exhausted T-cells are characterized by high levels of TIM-3
182 with reduced effector functions such as decreased cytokine production and cytotoxicity (65,
183 66). Overall, in terms of GP33+ PD-1+ T-cells, we observed an increase in stem-like TCF-1+
184 progenitors concurrent with a reduction in both transitory and terminal exhausted CD8+ T-
185 cells (**Fig. 1O**). The same TCF-1+ progenitors also showed an increase in cell division as
186 shown by Ki67 expression (**Fig. 1P**). Similar results were seen in an *in vitro* model of
187 exhaustion where splenic T cells were restimulated over 13 days (**Supplementary Figure**

188 **S3**). The GSK-3-/- Lck Cre T cells showed reduced levels of PD-1 and TIM-3 expression (**Fig**
189 **S3B**) and concurrently, a frequency of IFN-γ and TNF-α co-producing cells (**Fig S3C**).
190 Overall, these data show for the first time using a genetic knock-down model that GSK-3
191 plays a central role in the generation of stem-like progenitors in the process that limits T-cell
192 exhaustion.
193
194 **GSK-3KD induces metabolic reprogramming toward glycolysis in T-cells**
195 The increased presence of CD8+ progenitor and memory cells in dLCK-CRE infected
196 mice suggested that the mediator might control the sensitivity of T-cells to TCR ligation. To
197 assess this, isolated CD8+ T-cells were labelled with Tag-it and incubated in vitro with a
198 titration of soluble anti-CD3 antibodies from a range of 0.005 to 2ug/ml over 48-62 hours
199 (**Fig. 2A**). Under these conditions, the proliferative response between KD and WT T-cells
200 were similar. The one exception was the response to lowest concentration of 0.005ug/ml
201 anti-CD3 where the KD T-cells exhibited a clearly better response (see arrow). A similar
202 result was obtained when we stained for Ki67, a marker for cell division (**Fig. 2B**). This clearly
203 demonstrated that GSK-3 controls the sensitivity of T-cells to a remarkably low concentration
204 of anti-CD3. These data suggest that GSK-3 might eventually be found to protect against
205 responses to low affinity or abundance self-antigen.
206 T-cell activation involves a switch from oxidative phosphorylation to glycolysis (67-70).
207 The role of GSK-3 in T-cells has not been examined. We therefore measured oxygen
208 consumption rate (OCR) and extracellular acidification rate (ECAR) in resting and anti-CD3
209 stimulated T-cells at 24 hours using Seahorse XF24 Extracellular Flux Analyzer (**Fig. 2C-K**).
210 Cells were subjected to the sequential addition of mitochondria perturbing agents such as
211 oligomycin, to block ATP synthesis, FCCP to uncouple the electron transport chain, and
212 rotenone and antimycin A which block ETC complex I and III, respectively). ECAR as a
213 measure of glycolysis as shown in a representative experiment (**Fig. 2C**). Both basal and
214 anti-CD3 induced glycolysis with the addition of exogenous glucose was clearly higher GSK-
215 3 KD T-cells. Comparative measurements from different mice confirmed a significance in
216 glycolysis in response to anti-CD3 (**Fig. 2D**). In addition, the glycolytic capacity in the GSK-
217 3KD T cells was higher (**Fig. 2E**) and the glycolitic reserve (i.e., as indicated by the difference
218 between the maximal ECAR after glucose and oligomycin addition and maximal ECAR after
219 glucose injection only)(**Fig. 2F**). These data showed that the reduction of GSK-3 expression
220 augmented glycolysis as induced by anti-CD3.

221 GSK-3 levels also affected mitochondrial respiration (i.e., OXPHOS) levels as assessed
222 by the OCR response (**Fig. 2G-K**). Basal OCR levels was higher in GSK-3 KD T-cells (**Fig.**
223 **2G, H**) as was the response to FCCP (**Fig. 2G**). The addition of FCCP determine the
224 maximal uncoupled respiration rate, which is the maximum rate of oxygen consumption that
225 can be achieved when the mitochondrial respiration is completely uncoupled from ATP
226 synthesis. This is an indicator of the cell's ability to meet increased energy demands under
227 stress condition. Basal and anti-CD3 induced OCR was higher the GSK-3 KD cells (**Fig. 2G**),
228 while despite a trend, no statiscal difference in the maximal respiration OCR between GSK-3
229 KD and WT cells was seen (**Fig. 2H**). Lastly, the spare respiration capacity,as indicated by
230 the difference between the maximal OCR (after FCCP injection) and basal OCR was actually
231 decreased in anti-CD3e cells from GSK-3 KD mice (**Fig. 2J**). In keeping with this, an increase
232 of ATP production but a reduction in the OCR/ECAR ratio was observed in T-cells from GSK-
233 3 KD mice (**Fig. 2K)**.
234 In keeping with these findings, the OCR to ECAR ratio was lower in KD cells (**Fig. 2L)**.
235 Further, the glucose uptake in CD8, but not CD4 cells, was higher in KD T-cells (**Fig 2M**) as
236 was the expression of the glucose transporter-1 receptor (GLUT-1) (**Fig 2O).** GLUT-1 plays
237 a crucial role in facilitating glucose uptake in activated T-cells (71-73). Notably, this increased
238 expression was more pronounced in CD8+ T-cells (**Figs 2O and P**). Further, the elevated
239 GLUT-1 was observed in GP33+ CD8+ MPECs (**Fig 2Q**), but not in SLECs (**Fig. 2R**).
240 Overall, our findings indicated that GSK-3 affected both glycolysis and OXPHOS pathways in
241 cellular metabolism with a particularly strong impace on anti-CD3 glycolysis associated with
242 the MPEC subset of effector memory T-cells.
243
244 **GSK-3 empowers anti-PD1 to overcome ICB tumor resistance**
245 Given these combined effects, we next assessed the role of GSK-3 in regulating
246 CD4+CD8+ T-cell cooperation, where CD4+ T cells provide help needed for CD8+ T cells[57]. For
247 this, we derived and used a B16-F10 melanoma subclone (B16-F10 R1) which is resistance to
248 anti-PD-1 treatment. B16-F10 R1 cells were injected intradermally followed by intra-peritoneal
249 injections of SB415286 (GSK- 3 SMI), anti-PD1 or SB415286/anti-PD1 every 4 days (**Fig. 3A**).
250 Neither anti-PD-1 nor SB415286 monotherapy affected tumor growth (**Fig. 3B**). However, the
251 combination of anti-PD-1 and SB415286 synergized to reduce tumor growth from days 8-17
252 based on tumor volume (**Fig. 3B**) and tumor weight when measured at day 15 (**Fig 3C**). Spider-
253 graphs show reduced volume growth of individual tumors in mice (**Fig. 3D,** left panels). In

254 addition, 65% of mice bearing B16-F10 R1 tumors became responsive to combination therapy
255 as opposed to non with monotherapy (**Fig. 3D**, right panel).
256 To define TILs, we used Time-of-Flight (CyTOF) mass cytometry with a panel of 15
257 monoclonal antibodies (**Fig. 3E-L**). From this, 20 distinct cellular subsets within the anti-TCRβ
258 population became apparent as shown with phenograph illustrations (**Fig. 3E**), heat maps (**Fig.**
259 **3F**) and boxplot representations (**Fig. 3G**). Despite this, although there were various upward
260 and downward trends, only two clusters achieved statistical significance (<0.05)
261 (**Supplementary Figure S4**). Cluster 20 showed an increase which corresponded to a CD8+
262 subset with the phenotype CD44+IA-IE+CD11b-CD73-CD62L- and PDL1+ (p=0.013). This
263 effector CD8+ subset was negative for PD-1 and LAG-3 suggesting an absence of transitory or
264 terminal exhaustion (**Fig. 3F**). By contrast, Cluster 1 in the CD4+ subset showed a decrease
265 with the CD4+FoxP3+CD25+CD73+ suppressor phenotype (CD4+CD44+ CD25+, FoxP3+,
266 CD73+, PD-1+LAG3+ IA-IE+CD49F+PDL1+) (p=0.044).
267 Using a less stringent standard, there was a trend toward a decrease in the presence of
268 CD4 cells in Cluster 19, with a p-value of 0.09. Cluster 19 shared the expression of markers with
269 the Treg Cluster 1 but lacked expression of PD-1 and LAG3. FoxP3+ Cluster 12 was similar to
270 Cluster 19 but lacked expression of CD49F (integrin alpha 6) and had lower levels of CD73
271 inhibitory receptor CD73 (p value=0.127). Furthermore, CD8+ Cluster 4 showed an increase
272 with a p value of 0.149. It was like Cluster 20 but expressed exhaustion markers PD-1, LAG3,
273 and CD73. CD73 defines a highly suppressive Treg population (74, 75). Overall changes were
274 seen in an increase in CD8+ TILs and a decrease in various regulatory T cell (Treg) suppressor
275 due to combination therapy.
276 We also employed standard flow cytometry to complement the CyTOF readings (**Figs. 3H-**
277 **L**). This combined approached confirmed an increase in CD8 effector TILs (**Fig. 3H**) effector-
278 memory (EM) $CD8^+$ T-cells with combination therapy (**Fig. 3J**). Interestingly, increased
279 frequency of CD8+ EM TILs was correlated with a reduced tumor size (**Figs. 3K**). Surprisingly
280 by contrast, there was no correlation between CD8+ EFF TILs and tumor regression (**Fig. 3I**).
281 Analysis by both CyTOF and conventional flow cytometry revealed a decreasing trend in the
282 proportion of CD4+ tumor-infiltrating lymphocytes (TILs) **(Fig. 3L),** as well as a more
283 pronounced reduction in the CD4+$FOXP3^{hi}$ CD25+ regulatory T cell (Treg) population with
284 suppressive functions **(Fig. 3M).** Flow cytometry analysis using fluorescent antibody staining
285 corroborated the reduction in PD-1+ cells within the Treg population and further revealed a

286 decrease in the Treg population expressing TIM-3, for which metal-conjugated antibodies were
287 unavailable (**Supplementary Figure S5**).
288
289 **GSK-3 licenses anti-PD-1 blockade to induce perforin and 7/9 granzymes for enhanced**
290 **CD8+ CTL TILs**
291 We next proceeded to evaluate gene expression patterns induced by anti-PD-1 and GSK-
292 3 signaling through transcriptome profiling (**Figs. 4A-C**). Using a threshold of at least 2-fold
293 higher expression with $p<0.01$, a Venn diagram illustrated the genes differentially expressed
294 under GSK-3 inhibitor monotherapy, anti-PD-1 monotherapy, and combination therapy (**Fig.**
295 **4A**). We assessed control vs anti-PD1 monotherapy, control vs GSK-3i monotherapy, and
296 control vs combination therapy. The combination therapy group was further divided into genes
297 from tumors of highly responsive (i.e., termed responsive) and more poorly responsive (i.e.,
298 termed non-responsive), where responsive showed a greater than 50% reduction in tumor size
299 relative to the mean for untreated mice. Volcano plots showed an increase and decrease in
300 expression of different genes (x-axis shows the change magnitude while the y-axis shows
301 statistical significance). Anti-PD-1 and GSK-3i induced a unique set of genes (162 vs 109,
302 respectively), as well as an overlapping 3 genes. Combination therapy showed that the
303 inhibition of GSK-3 allowed anti-PD-1 immunotherapy to express additional genes. Within this
304 group, combination therapy induced 910 unique genes in the responsive mice and 176 unique
305 genes in the non-responsive mice. This approach demonstrated that GSK-3 inhibition licenses
306 anti-PD-1 blockade to induce a unique set of altered genes in immunotherapy. Further, the
307 gene regulatory network showed an enrichment of genes associated with immune activation
308 and inflammatory response pathways. (**Supplementary Figure S6**).
309 Due to the extensive gene list, we implemented a more stringent filter requiring a minimum
310 two-fold expression change and a $p < 0.001$ significance level (**Fig. 4B**). Under these
311 conditions, volcano plot analysis revealed limited positive gene induction by GSK-3 SMI
312 inhibition alone involving FasL (**Fig. 4B**). In contrast, while anti-PD-1 monotherapy negatively
313 impacted the expression of numerous genes such as VCam1, CXCL9, CXCL11, and others, it
314 positively affected only two genes, FasL and Gm8369 (upper panel). In contrast, the
315 combination of anti-PD-1 and GSK-3 SMI synergistically induced many more genes, both
316 negatively and positively (lower panel). Differences were also seen in TILs from responsive
317 and non-responsive mice (**Fig. 4C**).

318 With a focus on the upregulated 37 genes, we noted the induction of important genes such
319 as interleukin 2 inducible kinase (ITK) and the transcription factor Tox2. ITK regulates
320 cytokine production and T-cell differentiation (76), while Tox2 is required for metabolic
321 adaptation and tissue residency of immune cells (77). However, in addition was the
322 remarkable induction of perforin and 7/9 granzymes from within the mouse genome (**Fig. 4D**).
323 These included granzymes, GZMK, GZMG, GZME, GZMF, GZMD, GZMB and GZMC needed
324 for optimal CD8+ CTL killing function (**Fig. 4E**). Perforin is a pore forming cytolytic protein
325 found in the granules of CTLs, while granzymes enter via perforin to induce cell death (78, 79).
326 This effect is, to our knowledge, unprecedented.
327 In comparing the highly responsive (i.e., termed responsive) and poorly responsive (i.e.,
328 termed non-responsive) mice, the TILs from the poorly responding mice showed an increase
329 in the expression of GZMG, GZME, GZMF, and GZMD, but no significant increase in GZMK,
330 GZMB, or perforin expression (**Fig. 4F**). A trend to increase was observed but it was not
331 statistically significant. Perforin, a critical pore-forming protein essential for CTL-mediated
332 cytotoxicity, resides within cytotoxic granules and is influenced by PD-1 internalization (25).
333 Furthermore, GZMB has been previously demonstrated to play a pivotal role in CD8+ T cell
334 effector function of TILs (80).
335 To confirm the role of the lesser-known granzymes in CD8+ T-cell-mediated killing, siRNA
336 to down-regulate GZM D and F was assessed in an OT-1 CTL killing assay (**Fig. 4G**). OT-1 T-
337 cells were activated with anti-CD3/CD28 for 24 hours and electroporated with siRNAs targeting
338 both GZMD and GZMF. Cytotoxic CD8+ T cells were cultured for 48 hours before being used
339 in a killing assay against EL4 target cells. While a control siRNA with a fluorescent label (FITC-
340 scrambled) had minimal impact on killing activity, siRNAs targeting GZMD and GZMF reduced
341 killing by more than 20% compared to the FITC-scrambled control and cells without RNA
342 transfection (mock). These findings showed roles for GZMD and GZMF in the killing efficiency
343 of cytotoxic CD8+ T cells. Furthermore, building upon the previous analysis of TCF-1+ stem-
344 like T cells, the combined treatment of anti-PD-1 and GSK-3 SMI significantly increased *tcf7*
345 expression (**Fig. 4H**).
346
347 **GSK-3KD licenses anti-PD-1 induction of CD8 multi-granzyme expression**
348 These findings were further corroborated by comparing the response of WT vs GSK-3
349 KD mice to anti-PD1 blockade (**Fig. 5**). While anti-PD1 failed to significantly inhibit B16 F10
350 R1 tumor growth in WT mice, it reduced tumor growth by more than 75% in dLCK-CRE mice.

351 This was evident in both tumor volume (**Fig. 5A**) and by the measurement of tumor weight at
352 day 16 post-implantation (**Fig. 5B**). Further, flow cytometry analysis of a representative
353 experiment showed that anti-PD1 increased the frequency of CD8+ TILs from 37% to 46.3%
354 in WT mice (**Fig. 5C**). The increase in CD8+ TILs was further augmented to 60.2% in GSK-3
355 KD mice. Consistent with the increase in CD8+ T-cells, the total number of CD8+ TILs
356 increased in WT in response to anti-PD1 from 2.4 x 10^6 cells/g. However, in the KD mice, this
357 increased to 9.2 x 10^6 cells/g (**Fig. 5D**).
358 FACS staining of granzymes then showed that anti-PD-1 in GSK-3 KD mice significantly
359 upregulated the expression of perforin and multiple granzymes, GZMA, GZMB, GZMC, and
360 GZMF (as assessed by available anti-granzyme antibodies) (**Fig. 5E**). Other granzymes did
361 not have suitable antibodies which worked in flow cytometry. Nevertheless, while anti-PD1
362 monotherapy resulted in an increased frequency of GZMB-expressing CD8+ T-cells in WT
363 mice, combination of anti-PD-1 in GSK-3 KD mice significantly upregulated the expression of
364 perforin, GZMA, GZMB, GZMC, and GZMF in terms of mean fluorescence intensity (MFI) of
365 expression (upper panel) and the percentage of CD8+ T-cells expressing each granzyme
366 (lower panel). These data demonstrate that GSK-3 inhibition synergizes with anti-PD1
367 therapy to enhance the cytotoxic capacity of CD8+ T-cells by upregulating the expression of
368 a broad spectrum of granzymes, thereby facilitating more effective tumor eradication.
369

370 **GSK-3 alters CD4+ Treg vs T-help in tumors and regulates CD8+ CTL dependency on**
371 **CD4+ T cell help**

372 Given that CD8+ T-cell differentiation can be facilitated by CD4+ T-cell help (4-6), a key
373 next question was whether the induction of GZMs was due to a role of GSK-3 in regulating
374 CD4-CD8 cooperation where help is provided to CD8+ T-cells (**Fig. 6).** The downregulation
375 of GSK-3 did not affect the overall numbers of CD4+ TILs (**Fig. 6A**). It did however increase
376 the numbers of T-helper cells relative to CD4+ FoxP3+ suppressor cells in the TIL population
377 **(Fig. 6B**). In a representative FACs plot, anti-PD-1 therapy induced an increase in the
378 presence of CD4+ FoxP3+ regulatory TILs in WT mice from 36.8 to 59.8% of CD4+ CD44+
379 TILs, as reported (81-84). At the same time, the percentage of FoxP3 negative CD4+ TILs
380 decreased. In striking contrast, in dLck-CRE mice, anti-PD-1 cooperated to increase the
381 percentage of T-helper cells from 40.2 in WT to 73.8, while concurrently decreasing the
382 presence of Tregs from 59.8 in WT to 26.4%. These data, consistent with the CyTOF

383 analysis, showed that GSK-3 plays a pivotal role in regulating the relative presence of CD4+
384 T helper vs Treg TILs in response to anti-PD-1 therapy.
385 Further, anti-PD-1 treatment in dLCK-CRE mice also led to a significant reduction in both
386 the frequency and expression of the inhibitory receptor TIM3 on CD44+CD4+ TILs, as
387 demonstrated by flow cytometry analysis. This decrease in expression was evident in the
388 FACS plots (**Fig. 6C**) as reflected in a decrease in the percentage of TIM3+ cells (**Fig. 6D**),
389 and level of expression (i.e., MFI) (**Fig. 6E**). Tim-3 expression on CD4+ T-cells promotes T-
390 cell exhaustion, while expression of Treg cells correlates with greater suppressive ability (85).
391 Given the changes in the composition of the CD4 subset, we next depleted CD4 cells by
392 injecting mice at various time points to remove CD4+ T-cells before and during anti-PD-1
393 therapy. Interestingly, CD4 depletion allowed anti-PD-1 therapy to reject the B16-F10 R1
394 tumors in wild-type (WT) mice (**Fig. 6F**). This was evident from the reduced tumor volume
395 (**Fig. 6F**) and tumor weight (**Fig. 6G**). Since anti-PD-1 therapy alone was normally unable to
396 promote tumor rejection and typically increased the presence of regulatory T cells (Tregs),
397 these observations suggested that the loss of CD4+ Tregs through anti-CD4 depletion
398 enabled anti-PD-1 therapy to reject tumors, which was not observed when CD4+ T-cells were
399 present.
400 Conversely, in dLCK-CRE mice, with greater numbers of CD4 T-helpers, the depletion of
401 CD4 TILs caused a complete loss in the ability of anti-PD-1 to promote tumor rejection (**Fig.
402 6F, G**). This was seen both in tumor volume (**Fig. 6F**) and tumor weight (**Fig. 6G**). In this
403 scenario, anti-PD-1 lost its ability to promote an increase in the presence of CD8+ TILs as
404 shown in a representative FACs plots (**Fig. 6H**) or in terms of numbers of CD8+ T-cells/g of
405 tumor (**Fig. 6I**). In addition, the loss of CD4 help in the GSK-3 KD mice resulted in a complete
406 loss in the increase in the expression of the multiple granzymes in the CD8+ TIL population
407 (**Fig. 6J**). This loss was seen in terms of protein expression (i.e., MFI) (upper panel) and in
408 the percentage expression (lower panel) for perforin, GZMA, GZMB, GZMC and GZMF.
409 Confirmation that the suppression of the anti-tumor response due to the presence of
410 Tregs in the TIL population from WT mice was seen by the ability of anti-CTLA-4 depletion to
411 also allow a reduction in tumor size (**Fig. 6J**). Anti-CTLA-4 is effective in depleting CD4+
412 Tregs (86). By contrast, anti-CTLA-4 had no effect on the regression of the B16 F10 R1
413 tumor in the GSK-3KD mice. Since anti-CD4 did reverse the enhanced regression in tumors
414 in the dlck-CRE mice (**Fig. 6F**), these data indicate that the effect of anti-CD4 on tumor

415 regression in T-cells with reduced expression of GSK-3 was due to the loss of CD4+ T-helper
416 cells.
417 To test for a potential difference in dendritic cells (DCs), *in vitro* derived bone marrow
418 derived DCs from dLCK-CRE vs WT mice supplemented with granulocyte-macrophage
419 colony-stimulating factor (GM-CSF) were found to exhibit comparable surface antigen
420 expression profiles (**Supplementary Figure S7**). Overall, these results demonstrate that
421 GSK-3 expression plays a pivotal role in determining the relative presence of T-helper cells
422 versus Tregs in tumors in response to anti-PD-1 treatment and consistent with this, the
423 dependency of CD8+ T-cells on CD4+ T-cell help for their presence in tumors and their
424 expression of multiple granzymes needed for tumor killing.
425

426 **Discussion**

427 Despite its importance in T-cell signaling, the full role of GSK-3 in immune checkpoint
428 blockade has yet to be explored. In this study, we show that GSK-3 normally limits the ability of
429 anti-PD-1 to elicit the full development of CD8 CTL responses against tumors. Further, this
430 involves the regulation of the balance between the presence of regulatory and helper T-cells in
431 their regulation of CD8 expression of cytolytic granzymes needed to kill tumors. The genetic
432 knockdown of GSK-3 increased memory TCF-1+ T-cells with reduced overall exhaustion for more
433 potent anti-viral and tumor immunity. GSK-3 knockdown and inhibition licensed anti-PD-1 to
434 overcome tumor resistance in a process that down-regulated CD4+ Tregs while increasing the
435 presence of effector-memory CD8+ T-cells. This synergy resulted in the generation of super-
436 armed killer T-cells expressing an unprecedented 7/9 cytolytic granzymes (GZMs K, G, E, F, D,
437 B, C). Importantly, reduced GSK-3 expression was essential for CD4+ helper collaboration with
438 CD8+ T-cells to express these unprecedented numbers of cytolytic granzymes. Our findings offer
439 a novel therapeutic strategy for cancer immunotherapy, with the potential to improve treatment
440 outcomes by optimizing CD4-CD8 T-cell crosstalk needed to increase GZM expression.

441 Our initial findings showed that GSK-3 KD favored the generation of TCF1+ progenitor
442 memory cells. This feature was first seen in LCMV Cl13 infection, showing a continued increase
443 in both central and effector memory T-cells as well as a preferential increase in the presence of
444 MPECs relative to SLECs. MPECs play a key role in developing immunological memory to
445 respond to future infections (87, 88). This increase in TCF1+ progenitors in GSK-3 inhibited
446 conditions concurrently led to a reduction in T-cell exhaustion using in vivo and in vitro assays.
447 Small chemical inhibitors have previously used (89), although there have been no reports on the
448 connection between GSK-3 and memory progenitors using genetically altered CD4+ and CD8+
449 T-cells. A selective KO in CD8+ T-cells showed reduced exhaustion but failed to establish a link
450 to the generation of TCF-1+ progenitor T-cells (90). Surprisingly, the same subset showed an
451 increase in the expression of the cell cycle marker Ki67 in GSK-3 KD but not wild-type mice.
452 Further, in our study MPECs showed an increase in the expression of GLUT-1 and an increase in
453 glucose uptake. These observations place the GSK-3 kinase upstream in a signaling pathway in
454 the control of the generation of TCF-1+ progenitor memory T-cells (91, 92).

455 Since the presence of progenitor TCF-1+ T-cells is required for successful anti-PD-1 therapy
456 (26-28), we next tested whether GSK-3 inhibition with small molecule inhibitors (SMIs) or its
457 genetic downregulation could cooperate with anti-PD-1 in eliminating a tumor that is normally

458 resistant to checkpoint blockade. In the B16 F10 R1 model, tumor growth was unaffected by
459 monotherapy but was reduced by more than 70% when assessed on day 16 with the combination
460 treatment. Furthermore, tumor regression was associated with a significant shift in the tumor
461 microenvironment. Specifically, CyTOF analysis showed a loss of highly suppressive FOXP3hi
462 CD25+ Tregs concurrent with an increase in CD8+ effector (EFF) and effector memory (EM)
463 CD8+ TILs. The increase in EM cells in the tumor model was correlated with a reduction in tumor
464 mass. The lack of correlation with EFF CD8+ T-cells might relate to their more terminal
465 differentiation and shorter lifespan needed to sustain a response to tumor neoantigens. GSK-3
466 expression plays a central role in determining the relative presence of Tregs and CD8 effector
467 memory cells in tumors in response to anti-PD-1 therapy.
468 Transcriptomics also showed that GSK-3 down-regulation controlled the response of the T-
469 cells to anti-PD-1 by licensing blockade to regulate many more genes that normally induced by
470 anti-PA-1 alone. The effect was also selective as shown by a skewed effect in preferentially
471 affecting immune associated genes. Further, and of special interested was selective effect on the
472 unprecedented increase in the expression of granzymes needed to kill tumors. Of the 37 genes
473 induced by combination therapy, these included perforin, a pore-forming protein crucial for CTL
474 cytotoxicity (93), and 7/9 granzymes in the mouse genome. Therefore, at least 8 of 37 induced
475 genes were genes that controlled CTL killing. This included the well-known GZMB as well as less
476 well-studied granzymes GZMK, GZMG, GZME, GZMF, GZMD, and GZMC. Notably, cells
477 expressing high levels of GZMF are distinct from those expressing GZMA and GZMB in their
478 mechanism of eliminating cancer cells (31). GZMC and GZMK employ a different caspase-
479 independent pathway for killing (32). This upregulation of multiple granzymes is unprecedented in
480 the literature and indicative of a 'super-arming' of cytolytic T cells, enhancing their capacity for
481 tumor destruction.
482 To achieve this remarkable effect, we also uncovered the cellular mechanism by showing
483 that levels of GSK-3 expression determine the relative presence of T-helper cells versus Tregs
484 in tumors in response to anti-PD-1 treatment. Further, it determined the dependency of CD8+ T-
485 cells on CD4+ T-cell help for their presence in tumors for the expression of the multiple
486 granzymes needed for tumor killing. We observed an increase in the presence of Tregs seen in
487 WT mice in response to anti-PD-1 which failed to occur in GSK-3KD mice. Remarkably instead,
488 the reduced level of GSK-3 allowed anti-PD-1 to support the increased presence of CD4+FoxP3
489 negative helper TILs. In turn, anti-CD4 depletion experiments showed that this CD4+ T cell help
490 was needed for the regression of tumors, the increased presence of CD8+ TILs and crucially,

491 for inducing the multiple GZMs including GZMK, GZMG, GZME, GZMF, GZMD, and GZMC
492 machinery of GSK-3 KD CD8+ CTLs. This suggests that GSK-3 is a key player in the
493 development of poorly performing CD8 T-cells in the absence of CD4 T-cell help (4, 5, 7)..
494 The depletion of Tregs with anti-CTLA-4, in turn, mirrored the effect of anti-CD4 in allowing
495 WT mice to clear the tumor. This showed that the anti-CD4 depletion effects were most likely
496 related to its depletion of Tregs in WT mice, which normally suppresses tumor clearance.
497 However, in the case of the dLckCre mice with reduced levels of GSK-3 and the reduced
498 presence of Tregs, anti-CTLA-4 had no effect on the enhanced ability of the mice to regress
499 tumors. This supports the notion that anti-CD4 reversed tumor size reduction in dLckCre mice
500 by eliminating CD4+ helper T-cells. This pathway by which GSK-3 controls anti-PD-1 effects on
501 CD4-CD8 cooperation for the relative presence of suppression versus help and the
502 development of super-armed CD8+ TILs is a new pathway in the regulation of tumor
503 immunotherapy.
504 One contributing factor not yet reported is that the reduction in GSK-3 caused T-cells to be
505 more reliant on glycolysis relative to oxidative phosphorylation for their energy requirements. The
506 effect on extracellular acidification rate (ECAR) was more striking than on the oxygen
507 consumption rate (OCR) with a lower OCR/ECAR ratio. This reliance on glucose uptake was also
508 evident with the greater glucose uptake and GLUT-1 expression on GSK-3 KD cells, where this
509 effect was most evident in GP33+ CD8+ MPECs. This observation, combined with the greater
510 cell division evident in MPECs, as seen with Ki67 expression (data not showed), is consistent
511 with the shift in T-cells from the primarily use of oxidative phosphorylation to glycolysis upon
512 activation (94, 95). In addition, stem-like progenitor T-cells primarily utilize glycolysis to generate
513 ATP (96). Although not reported before for T-cells, B-cell responses to the co-stimulatory receptor
514 CD40 also engage glycolysis (97). In another study, IL-24 has been reported to inhibit GSK3β is
515 mediated through PKA activation, activating glycogen synthase and decreasing intracellular
516 glucose levels (98).
517 Overall, our findings in this paper related to GSK-3 regulation of CD4-CD8 collaboration in
518 the generation of CD8 CTLs could provide a mechanism to explain the past findings showing that
519 GSK-3 can promote CAR function and tumor rejection (42, 54-56, 59-61). The one exception was
520 the generation of mice using a granzyme B (GZMB)-Cre for GSK-3 deletion that showed an
521 increase in tumor growth (90). However, this difference may relate to the fact that the GZMB-Cre
522 system also targets NK cells and cytolytic CD4+ T cells, regulatory suppressor CD4+ T cells
523 (Tregs), Group 1 ILCs, mast cells, and macrophages (99). Overall, our findings underscore the

importance of the serine/threonine kinase GSK-3 in governing the nature of the immune response in checkpoint blockade, both in terms of its control of the cooperation between CD4 and CD8 T-cells and enhanced GZM expression in anti-PD-1 therapy.

Acknowledgements

We thank Dale long and his team from NIH Tetramer Core Facility at Emory for providing GP33 tetramers and Fredéric Duval and Anne-Mari Aubin from the Flow Cytometry Core Facility of CR-HMR for their help. This project was supported by the Canadian Institutes of Health Research Foundation grant (159912) (PI) and National Institutes of Health grant RO1 AI049466 (co-PI). CER holds a majority stake in ImmunoAb Res Inc (Canada).

Methods

Ethic approval

Animal experiments were approved by the Animal Care Use and Review Committee of Center Research -Hospital Maisonneuve Rosemont (CR-HMR) (ethical approval no 2021-2516, 2023-3032 and 2024-3547) from University of Montreal. For mouse tumor experiments, all tumor sizes/burdens were permitted by the CR-HMR of Montreal University. Maximal tumor burden permitted by the CR-HMR (1.5 cm3) was not exceeded in this study.

Key resources

A complete list of the reagents and antibodies used in this manuscript can be found in supplementary table S1.

Animals

Generation and Utilization of GSK-3αflox/flox βflox/flox mice

Two generations of GSK-3αflox/flox βflox/flox mice were produced: one in Montreal and another in our laboratory at the University of Cambridge, UK. The mice generated in Montreal were used exclusively for most experimental procedures. Splenocytes from the University of Cambridge were transported to the University of Leeds, courtesy of Dr. Alison Taylor, who kindly arranged their overnight shipment on ice to Montreal. These splenocytes were utilized in Supplementary

554 Figure 3. GSK-3αflox/flox and βflox/flox mice were crossed to generate double-negative mice in
555 Montreal. For both the Montreal and Cambridge cohorts, GSK-3αflox/flox βflox/flox mice were
556 bred with distal dLCK-Cre mice (B6.Cg-Tg(Lck-icre)3779Nik/J, Jackson Laboratory, Maine) to
557 delete both GSK-3α and GSK-3β isoforms. However, in the case of the Montreal mice, the
558 deletion was incomplete, resulting in the creation of GSK-3 knock-down mice. All mice were
559 maintained in an animal facility with a 12-hour light-dark cycle and had unrestricted access to
560 food and water throughout the study. The study adhered to ethical guidelines for animal
561 research. Sex was not a factor in the study design or analysis, as the study was not intended to
562 investigate sex differences.

563 Viral infections

564 LCMV Armstrong and Clone 13 strains were propagated in BHK-21 cells and their titers
565 determined using a plaque assay on Vero cells (100). Mice were infected with either LCMV
566 Armstrong via intraperitoneal (i.p.) injection at a dose of 2×10^5 plaque-forming units (PFU)
567 or with LCMV Clone 13 via intravenous (i.v.) injection at the same dose. Following infection,
568 mice were sacrificed at either day 7 (for LCMV Armstrong) or day 30 (for LCMV Clone 13) to
569 assess the effects of infection.

570 Cell lines

571 B16F10 tumor cells were maintained in DMEM supplemented with 10% FCS, 1% L-glut and 1%
572 Pen/Strep. Tumor cells ($2x10^5$) cultured for less than two weeks were implanted subcutaneously
573 in the flank of recipient mice using 29G1/2 syringes. Tumor size was monitored using a manual
574 caliper and tumors were excised before exceeding the volume permitted by CR-HMR ethic
575 committee.
576

577 Spleen Processing and T Cell Activation

578 Spleens were harvested from 8- to 16-week-old mice and mechanically dissociated in a 6-well
579 plate containing 2 mL of red blood cell lysis buffer (ACK buffer). An additional 2 mL of lysis
580 buffer was added, followed by a 5-minute incubation at room temperature. The reaction was
581 quenched with 20 mL of phosphate-buffered saline (PBS), and the suspension was filtered
582 through a 70 µm cell strainer. Cells were pelleted by centrifugation at 350 × *g* for 5 minutes.

583 Splenocyte pellets were resuspended in 1 mL of FACS buffer (PBS supplemented with 2 mM
584 EDTA and 2% fetal bovine serum [FBS]). Viable cells were quantified by Trypan blue exclusion

585 using a Neubauer hemocytometer. CD3+ T cells were isolated via magnetic bead-based
586 negative selection (StemCell Technologies). Following isolation, 2×10^6 T cells/mL were seeded
587 in 1 mL of activation medium (RPMI-1640 with L-glutamine, 10% FBS, 1 M HEPES, and 0.1%
588 β-mercaptoethanol) in a 48-well plate. Cells were activated with 1 μg/mL anti-CD3ε antibody
589 (clone 145-2C11) for 24 hours at 37°C under standard culture conditions.

590 Antibody Administration Protocol

591 Anti-PD-1 antibodies (Leinco) and SB415286 (Selleckchem) were reconstituted at 1 mg/mL
592 in sterile phosphate-buffered saline. Mice were administered 200 μg of the antibody solution
593 via intraperitoneal injection every 48 hours, starting on day 6 post-tumor implantation and
594 continuing until tumor resection on day 16[1].

595 CD4+ and CTLA-4 T-cell Depletion

596 To deplete CD4+ T cells, mice received 300μg of anti-CD4 antibody (Leinco) via
597 intraperitoneal injection 24 hours prior to tumor implantation (day -1), with subsequent
598 doses administered on days 7 and 14 post-implantation. This regimen ensured sustained
599 depletion throughout the experimental timeline. The small regime was used in the depletion
600 of Tregs with anti-CTLA-4. C57BL/6 mice were injected with 1×10^5 B16F10 melanoma
601 cells. In the αCTLA4 groups, mice received 200 μg of CTLA4 (clone 9d9) blocking antibody
602 (Leinco) IP at 4, 7, and 10 days thereafter. Tumors were measured by caliper every three
603 days, and tumor volume was calculated as length x width x width/2. At the time of sacrifice
604 for analysis, mice were euthanized using CO2 and subsequent cervical dislocation.

605 Glucose Uptake and Metabolic Profiling in Activated T Cells

606 Splenocytes were isolated and activated with 1 μg/mL anti-CD3ε antibody (clone 145-2C11)
607 for 48 hours at 37°C under standard culture conditions. For glucose uptake assessment,
608 activated cells were incubated with 2-NBDG (Thermo Fisher Scientific, #N13195) at a 1:1,000
609 dilution in phosphate-buffered saline (PBS) for 1 hour at 37°C, followed by fluorescence
610 quantification via flow cytometry.

611 Seahorse XF24 Metabolic Analysis

612 Oxygen consumption rate (OCR) and extracellular acidification rate (ECAR) were measured
613 using an Agilent Seahorse XF24 Extracellular Flux Analyzer. T cells were isolated, activated
614 as above, and seeded onto Cell-Tak-coated Seahorse cell culture plates. Prior to analysis,

615 cells were equilibrated for 90 minutes in Seahorse assay medium supplemented with 10 mM
616 glucose and 1 mM sodium pyruvate[3][4].

617 Mitochondrial respiration was evaluated using the Mito Stress Test Kit with sequential injection
618 of 0.5 μM rotenone/antimycin A (Rot/AA) and 2-NBDG (50 μM). Glycolytic capacity was
619 assessed via the Glycolytic Rate Assay Kit using 1.5 μM oligomycin, 2 μM carbonyl cyanide-4-
620 (trifluoromethoxy)phenylhydrazone (FCCP), and 0.5 μM Rot/AA[5][4]. Data were normalized to
621 cell density (2×10^5 cells/well) and analyzed using Wave software (Agilent Technologies)[3][6].

622 Reagents and antibodies

623 A complete list of the reagents and antibodies used in this manuscript can be found in
624 supplementary table S1.

625

626 Cell Preparation and Immunophenotyping

627 Organs were harvested from 8- to 16-week-old mice. Inguinal lymph nodes (LN) and thymus
628 were mechanically dissociated through a 70 μm cell strainer using the plunger of a 5 mL
629 syringe. The strainer was washed with 5 mL of FACS buffer (PBS supplemented with 10 mM
630 EDTA and 2% fetal bovine serum [FBS]). Tumors were mechanically disrupted on 70 μm
631 strainers in RPMI medium on ice. Tumor lysates were centrifuged at 350 × *g* for 5 minutes and
632 resuspended in PBS. The tumor lysate in PBS was layered onto lymphocyte separation
633 medium (Corning) and centrifuged at 2000 rpm for 20 minutes at room temperature to isolate
634 tumor-infiltrating lymphocytes (TILs).

635 Cell Blocking and Staining

636 Isolated cells from spleen, LN, thymus, and tumor were blocked with 100 μL of PBS containing
637 10 mM EDTA, 5% FBS, and 2.5 ng/mL purified rat anti-mouse CD16/CD32 (BD Biosciences
638 #553141) for 20 minutes at 4°C. Cells were then centrifuged at 350 × *g* for 5 minutes and
639 stained with primary antibodies (as detailed in the supplementary table) for 30 minutes at 4°C.
640 Each staining mix was supplemented with 1/1000 Fixable Viability Dye eFluor™ 780.
641 Following staining, cells were fixed with 2% paraformaldehyde (PAF) for 15 minutes at 4°C,
642 washed twice with PBS/10 mM EDTA + 2% FBS, and then permeabilized using the FOXP3 kit
643 (BioLegend) for 30 minutes at 4°C. Cells were stained with antibodies targeting intracellular
644 proteins, diluted in permeabilization buffer, for 50 minutes at room temperature. After staining,
645 cells were washed twice with PBS/10 mM EDTA + 2% FBS.

646 Flow Cytometric Analysis

647 Cell suspensions were analyzed using a BD LSRFortessa flow cytometer. Mean fluorescence
648 intensity (MFI) of specific markers was quantified on T cell subpopulations using FlowJo
649 software (Tree Star, Ashland, USA). Results were further analyzed using FlowJo to assess
650 immunophenotypic profiles.

651 Immunoblotting

652 Cell lysates were prepared by resuspension of spleen-purified CD8+ T cells in 1% Triton X-
653 100 lysis buffer, followed by a 30-min incubation on ice as described (101). Lysates were
654 centrifuged at 14,000 rpm for 30 min at 4°C and the nuclear-free supernatants were
655 subjected to SDS-PAGE on a 10 % polyacrylamide gel. Proteins from the gel were
656 electroblotted onto nitrocellulose membranes at 100V for 75 min, followed by 1 h of blocking
657 with 3% BSA in TBST at RT. The nitrocellulose membranes were then incubated in the
658 presence of the indicated primary Abs, followed by incubation with HRP-conjugated
659 secondary Abs. Immunoreactive protein bands were visualized using an ECL reagent and
660 autoradiography. Whenever required, nitrocellulose membranes were stripped by incubation
661 in stripping buffer for 20 min at RT, followed by 1 h incubation with blocking buffer (3% BSA
662 in TBST).

663

664 Mass cytometry (CyTOF)

665 Mass cytometry (CyTOF) analysis was performed at the McGill University CyTOF facility
666 following standardized protocols. Single-cell suspensions (3×10^6 cells) were stained with 5μM
667 Cell-ID™ Cisplatin (Fluidigm, San Francisco, CA) for viability assessment, followed
668 by32quenching with MaxPar® Cell Staining Buffer at a 5:1 volume ratio. Following
669 centrifugation (300g, 5 min, 4°C), cells were resuspended in 50 μL buffer and incubated with
670 human Fc receptor blocking solution (5 μL; BioLegend, San Diego, CA) for 10 minutes at
671 room temperature. Surface marker staining was performed using 50 μL of pre-titrated metal
672 conjugated antibody cocktail for 30 minutes (detailed panel composition in Reference 20).
673 After washing, cellular DNA was labeled overnight at 4°C using 1 mL intercalation solution
674 containing 125 nM MaxPar® Intercalator-Ir in MaxPar® Fix and Perm Buffer. Prior to data
675 acquisition, cells were washed with MaxPar® Water, resuspended with EQ™ Four Element
676 Calibration Beads, and analyzed on a Helios™ CyTOF II mass cytometer. A minimum of
677 100,000 viable single cells were acquired per sample at an event rate of 300-500

events/second. Analysis was performed on using antibodies against CD45, TCR-beta as indicated in Figure 4A.

Mass cytometry data analysis

Mass cytometry data analysis was performed using the Cytobank platform (Cytobank Inc., Mountain View, CA) following previously established protocols94, 95. All samples underwent simultaneous normalization and analysis to minimize technical variation and account for signal drift during extended acquisition periods. A standardized high-level gating strategy was implemented across all CyTOF files, incorporating sequential gates for event length, bead exclusion, cell viability, and DNA content. For comprehensive analysis, individual sample files were concatenated into a single dataset, from which population-specific data were subsequently extracted and separated into individual files for comparative analyses. Dimensional reduction was performed using t-Distribution Stochastic Neighbor Embedding (tSNE) analysis, which generated a two-dimensional representation (tSNE1 versus tSNE2) of the high-dimensional data by preserving local phenotypic relationships between cells, enabling visualization and identification of distinct cell populations based on their marker expression profiles.

Sample preparation for RNAseq and RNA profiling

Tumor was prepared as previously described and CD8+ TILs were isolated (Stemcell Technologies) RNA was isolated using the miRNeasy Mini Kit (Qiagen), and the mRNA was purified from 1ug of total RNA using the Dynabeads mRNA DIRECT Micro Kit (Thermo Fisher Scientific). The reverse transcription used SuperScript VILO cDNA Synthesis kit (Thermo Fisher Scientific). The whole transcriptome libraries were prepared using the Ion Total RNA-Seq Kit version 2 Kit (Thermo Fisher Scientific). The yield and size distribution of the amplified libraries were assessed with Agilent Bioanalyzer using Ion AmpliSeq transcriptome Mouse gene expression Kit (Thermo Fisher Scientific). Sequencing was performed on an Ion Proton Instrument (Ion Torrent, Thermo Fisher Scientific). RNA-sequencing (RNA-seq) analysis was done using the Torrent Suite software version 5.4.0 and the RNASeqAnalysis plugin (Thermo Fisher Scientific) on the mouse reference genome mm10 using STAR. Gene level expression is calculated using HTSeq and Picard to report raw read counts and FPKM (fragment per kilobase of transcript per million).

710

711 Cytolytic assay

712 EL4 cells (Target) were cultivated in RPMI + 10%FBS and incubated at RT for 25 min with
713 Tag-it 1/1000.Then, EL4 cells were pulsed with 1 µg/ml of OVA peptide at 37°C for 1 hour.
714 OT1 splenocytes (Effector) were isolated as previously described and activated with Anti-
715 CD28 2ug/mL + IL-2 5ng/mL and anti-CD3e 2ug/mL in activation media for 1 day at 37°C.
716 Effector cell were electroporated with 125nM of GZM siRNA or Ctrl siRNA and cultivated
717 overnight in RPMI+20% FBS+2%L-Glutamine+anti-CD3 (2ug/mL) and anti-CD28 (2ug/mL) +
718 IL2 (5ng/mL). Next day, cells were spin down at 300g for 5min, resuspended at the
719 concentration of 10^6/mL and cultivated for 24h in activated media + IL2 (50IU/mL). Next day
720 25000 of target cell were co-cultured for 6 days in activation media with 250000 effector
721 electroporated cells; Ration (E:T)=10:1 and dead percentage of target cell (Tag-it +) were
722 analysed in facs using a viability dye.

723

724 Bone marrow cultures with GM-CSF

725 Bone marrow cells, at a concentration of 10^6 cells per well, were seeded into 6-well
726 tissue culture plates, each containing 4 ml of medium consisting of RPMI 1640,
727 supplemented with glutamine, penicillin, streptomycin, 2-mercaptoethanol (all from
728 Invitrogen), 10% heat-inactivated fetal calf serum and GM-CSF at 20 ng/ml (Peprotech)
729 according to Helft et al 2015 (102). This culture was incubated at various days to generate a
730 dendritic cell enriched population. On day 2, 2 ml of the existing medium was removed and
731 replaced with 2 ml of fresh media with GM-CSF. On day 3, all medium was replaced with 4
732 ml of fresh medium containing 20 ng/ml GM-CSF. In some experiments, IL-4 (Peprotech)
733 was added to the medium at a concentration of 5 ng/ml, along with GM-CSF. On day 6-8,
734 non-adherent cells from the culture supernatant and the loosely adherent cells were
735 harvested by gentle washing with PBS, were collected and combined.

736

737 Statistical analysis

738 Respect of the assumptions of normal distribution of residuals and homoscedasticity was
739 verified, and data were presented as mean + SEM as well as individual values, unless
740 otherwise indicated. Data from independent experiments were pooled for analysis in each
741 data panel, unless otherwise indicated. Statistical analyses were performed using Prism 8

742 (GraphPad Software). Two-ways unpaired *t* test was performed unless otherwise indicated in
743 the figure legends. We considered a P-value lower than 0,05 as significant. N.S.: $P>0,05$; *:
744 $P<0,05$; **: $P<0,01$; ***: $P<0,001$; ****$P<0,0001$.
745
746 **Data availability statement**
747
748 Data sharing is not applicable as data for which a community-recognized, structured
749 repository exist (e.g. next-generation sequencing data) were not created or analyzed in this
750 study.
751
752

753

754 ReferencesAuthor, Title|. Journal| Year|. Volume|: Pages|.

755

756 1. Kalia V, Sarkar S, Ahmed R. Fine-tuning CD4+ central memory T cell heterogeneity
757 by strength of stimulation. European journal of immunology. 2008;38(1):15-9.
758 2. Topchyan P, Lin S, Cui W. The Role of CD4 T Cell Help in CD8 T Cell Differentiation
759 and Function During Chronic Infection and Cancer. Immune Netw. 2023;23(5):e41.
760 3. Laidlaw BJ, Craft JE, Kaech SM. The multifaceted role of CD4(+) T cells in CD8(+) T
761 cell memory. Nat Rev Immunol. 2016;16(2):102-11.
762 4. Aubert RD, Kamphorst AO, Sarkar S, Vezys V, Ha SJ, Barber DL, et al. Antigen-
763 specific CD4 T-cell help rescues exhausted CD8 T cells during chronic viral infection.
764 Proceedings of the National Academy of Sciences of the United States of America.
765 2011;108(52):21182-7.
766 5. Battegay M, Moskophidis D, Rahemtulla A, Hengartner H, Mak TW, Zinkernagel RM.
767 Enhanced establishment of a virus carrier state in adult CD4+ T-cell-deficient mice. J Virol.
768 1994;68(7):4700-4.
769 6. Borst J, Ahrends T, Babala N, Melief CJM, Kastenmuller W. CD4(+) T cell help in
770 cancer immunology and immunotherapy. Nat Rev Immunol. 2018;18(10):635-47.
771 7. Zajac AJ, Blattman JN, Murali-Krishna K, Sourdive DJ, Suresh M, Altman JD, et al.
772 Viral immune evasion due to persistence of activated T cells without effector function. J Exp
773 Med. 1998;188(12):2205-13.
774 8. Oh DY, Kwek SS, Raju SS, Li T, McCarthy E, Chow E, et al. Intratumoral CD4(+) T
775 Cells Mediate Anti-tumor Cytotoxicity in Human Bladder Cancer. Cell. 2020;181(7):1612-25
776 e13.
777 9. Mikami N, Sakaguchi S. Regulatory T cells in autoimmune kidney diseases and
778 transplantation. Nat Rev Nephrol. 2023;19(9):544-57.
779 10. Tay C, Tanaka A, Sakaguchi S. Tumor-infiltrating regulatory T cells as targets of
780 cancer immunotherapy. Cancer Cell. 2023;41(3):450-65.
781 11. Wood KJ, Sakaguchi S. Regulatory T cells in transplantation tolerance. Nat Rev
782 Immunol. 2003;3(3):199-210.
783 12. McLane LM, Abdel-Hakeem MS, Wherry EJ. CD8 T cell exhaustion during chronic
784 viral infection and cancer. Annu Rev Immunol. 2019(26).

785 13. Hudson WH, Gensheimer J, Hashimoto M, Wieland A, Valanparambil RM, Li P, et al.
786 Proliferating Transitory T Cells with an Effector-like Transcriptional Signature Emerge from
787 PD-1(+) Stem-like CD8(+) T Cells during Chronic Infection. Immunity. 2019;51(6):1043-58
788 e4.
789 14. Chen Z, Ji Z, Ngiow SF, Manne S, Cai Z, Huang AC, et al. TCF-1-Centered
790 Transcriptional Network Drives an Effector versus Exhausted CD8 T Cell-Fate Decision.
791 Immunity. 2019;51(5):840-55 e5.
792 15. Lin WW, Nish SA, Yen B, Chen YH, Adams WC, Kratchmarov R, et al. CD8(+) T
793 Lymphocyte Self-Renewal during Effector Cell Determination. Cell Rep. 2016;17(7):1773-
794 82.
795 16. Pais Ferreira D, Silva JG, Wyss T, Fuertes Marraco SA, Scarpellino L, Charmoy M,
796 et al. Central memory CD8(+) T cells derive from stem-like Tcf7(hi) effector cells in the
797 absence of cytotoxic differentiation. Immunity. 2020;53(5):985-1000 e11.
798 17. Gullicksrud JA, Li F, Xing S, Zeng Z, Peng W, Badovinac VP, et al. Differential
799 Requirements for Tcf1 Long Isoforms in CD8(+) and CD4(+) T Cell Responses to Acute
800 Viral Infection. J Immunol. 2017;199(3):911-9.
801 18. Lin WH, Adams WC, Nish SA, Chen YH, Yen B, Rothman NJ, et al. Asymmetric
802 PI3K Signaling Driving Developmental and Regenerative Cell Fate Bifurcation. Cell Rep.
803 2015;13(10):2203-18.
804 19. Baumeister SH, Freeman GJ, Dranoff G, Sharpe AH. Coinhibitory Pathways in
805 Immunotherapy for Cancer. Annu Rev Immunol. 2016;34:539-73.
806 20. Sharma P, Siddiqui BA, Anandhan S, Yadav SS, Subudhi SK, Gao J, et al. The Next
807 Decade of Immune Checkpoint Therapy. Cancer Discov. 2021;11(4):838-57.
808 21. Curran MA, Montalvo W, Yagita H, Allison JP. PD-1 and CTLA-4 combination
809 blockade expands infiltrating T cells and reduces regulatory T and myeloid cells within B16
810 melanoma tumors. Proc Natl Acad Sci U S A. 2010;107(9):4275-80.
811 22. Ott PA, Hodi FS, Robert C. CTLA-4 and PD-1/PD-L1 blockade: new
812 immunotherapeutic modalities with durable clinical benefit in melanoma patients. Clinical
813 cancer research : an official journal of the American Association for Cancer Research.
814 2013;19(19):5300-9.
815 23. Nguyen LT, Ohashi PS. Clinical blockade of PD1 and LAG3--potential mechanisms
816 of action. Nat Rev Immunol. 2015;15(1):45-56.

817 24. Rudd CE, Krueger J, Taylor A. Exploiting intracellular pathways of co-receptor
818 expression in the future of immunotherapy. Nat Rev Immunol. 2019;in press.
819 25. Ben Saad E, Oroya A, Anto NP, Bachais M, Rudd CE. PD-1 endocytosis unleashes
820 the cytolytic potential of checkpoint blockade in tumor immunity. Cell Rep.
821 2024;43(11):114907.
822 26. Siddiqui I, Schaeuble K, Chennupati V, Fuertes Marraco SA, Calderon-Copete S,
823 Pais Ferreira D, et al. Intratumoral Tcf1(+)PD-1(+)CD8(+) T cells with stem-like properties
824 promote tumor control in response to vaccination and checkpoint blockade immunotherapy.
825 Immunity. 2019;50(1):195-211 e10.
826 27. Sade-Feldman M, Jiao YJ, Chen JH, Rooney MS, Barzily-Rokni M, Eliane JP, et al.
827 Resistance to checkpoint blockade therapy through inactivation of antigen presentation. Nat
828 Commun. 2017;8(1):1136.
829 28. Miller BC, Sen DR, Al Abosy R, Bi K, Virkud YV, LaFleur MW, et al. Subsets of
830 exhausted CD8(+) T cells differentially mediate tumor control and respond to checkpoint
831 blockade. Nat Immunol. 2019;20(3):326-36.
832 29. Barry M, Bleackley RC. Cytotoxic T lymphocytes: all roads lead to death. Nat Rev
833 Immunol. 2002;2(6):401-9.
834 30. Cullen SP, Brunet M, Martin SJ. Granzymes in cancer and immunity. Cell Death
835 Differ. 2010;17(4):616-23.
836 31. Hay ZLZ, Kim DD, Cimons JM, Knapp JR, Kohler ME, Quansah M, et al. Granzyme
837 F: Exhaustion Marker and Modulator of Chimeric Antigen Receptor T Cell-Mediated
838 Cytotoxicity. J Immunol. 2024;212(8):1381-91.
839 32. Johnson H, Scorrano L, Korsmeyer SJ, Ley TJ. Cell death induced by granzyme C.
840 Blood. 2003;101(8):3093-101.
841 33. Rudd CE. How the Discovery of the CD4/CD8-p56(lck) Complexes Changed
842 Immunology and Immunotherapy. Front Cell Dev Biol. 2021;9:626095.
843 34. Samelson LE. Signal transduction mediated by the T cell antigen receptor: the role
844 of adapter proteins. Annu Rev Immunol. 2002;20:371-94.
845 35. Cantrell D. Signaling in lymphocyte activation. Cold Spring Harb Perspect Biol.
846 2015;7(6).
847 36. Rudd CE. Adaptors and molecular scaffolds in immune cell signaling. Cell.
848 1999;96(1):5-8.

849 37. Courtney AH, Shvets AA, Lu W, Griffante G, Mollenauer M, Horkova V, et al. CD45
850 functions as a signaling gatekeeper in T cells. Sci Signal. 2019;12(604).
851 38. Barber EK, Dasgupta JD, Schlossman SF, Trevillyan JM, Rudd CE. The CD4 and
852 CD8 antigens are coupled to a protein-tyrosine kinase (p56lck) that phosphorylates the CD3
853 complex. Proc Natl Acad Sci U S A. 1989;86(9):3277-81.
854 39. Wei Q, Brzostek J, Sankaran S, Casas J, Hew LS, Yap J, et al. Lck bound to
855 coreceptor is less active than free Lck. Proc Natl Acad Sci U S A. 2020.
856 40. Chan AC, Iwashima M, Turck CW, Weiss A. ZAP-70: a 70 kd protein-tyrosine kinase
857 that associates with the TCR zeta chain. Cell. 1992;71(4):649-62.
858 41. Sharma S, Quintana A, Findlay GM, Mettlen M, Baust B, Jain M, et al. An siRNA
859 screen for NFAT activation identifies septins as coordinators of store-operated Ca2+ entry.
860 Nature. 2013;499(7457):238-42.
861 42. Taylor A, Harker JA, Chanthong K, Stevenson PG, Zuniga EI, Rudd CE. Glycogen
862 synthase kinase 3 inactivation drives T-bet-mediated downregulation of co-receptor PD-1 to
863 enhance CD8(+) cytolytic T cell responses. Immunity. 2016;44(2):274-86.
864 43. Woodgett JR. Molecular cloning and expression of glycogen synthase kinase-
865 3/factor A. EMBO J. 1990;9(8):2431-8.
866 44. Doble BW, Woodgett JR. GSK-3: tricks of the trade for a multi-tasking kinase. J Cell
867 Sci. 2003;116(Pt 7):1175-86.
868 45. Rayasam GV, Tulasi VK, Sodhi R, Davis JA, Ray A. Glycogen synthase kinase 3:
869 more than a namesake. Br J Pharmacol. 2009;156(6):885-98.
870 46. Frame S, Cohen P. GSK3 takes centre stage more than 20 years after its discovery.
871 Biochem J. 2001;359(Pt 1):1-16.
872 47. Hughes K, Nikolakaki E, Plyte SE, Totty NF, Woodgett JR. Modulation of the
873 glycogen synthase kinase-3 family by tyrosine phosphorylation. Embo J. 1993;12(2):803-8.
874 48. Woodgett JR. Molecular cloning and expression of glycogen synthase kinase-
875 3/factor A. Embo J. 1990;9(8):2431-8.
876 49. Eldar-Finkelman H, Martinez A. GSK-3 inhibitors: preclinical and focus on CNS.
877 Front Mol Neurosci. 2011:doi: 10.3389/fnmol.2011.00032.
878 50. Embi N, Rylatt DB, Cohen P. Glycogen synthase kinase-3 from rabbit skeletal
879 muscle. Separation from cyclic-AMP-dependent protein kinase and phosphorylase kinase.
880 European journal of biochemistry / FEBS. 1980;107(2):519-27.

881 51. Beurel E, Grieco SF, Jope RS. Glycogen synthase kinase-3 (GSK3): regulation,
882 actions, and diseases. Pharmacol Ther. 2015;148:114-31.
883 52. Gounari F, Khazaie K. TCF-1: a maverick in T cell development and function. Nat
884 Immunol. 2022;23(5):671-8.
885 53. Zhao P, Sun L, Zhao C. TCF1/LEF1 triggers Wnt-dependent chemokine/cytokine-
886 induced inflammation and cadherin pathways to drive T-ALL cell migration. Biochem
887 Biophys Rep. 2023;34:101457.
888 54. Taylor A, Rudd CE. Glycogen synthase kinase 3 (GSK-3) controls T-cell motility and
889 interactions with antigen presenting cells. BMC Res Notes. 2020;13(1):163.
890 55. Rudd CE, Chanthong K, Taylor A. Small Molecule Inhibition of GSK-3 Specifically
891 Inhibits the Transcription of Inhibitory Co-receptor LAG-3 for Enhanced Anti-tumor
892 Immunity. Cell Rep. 2020;30(7):2075-82 e4.
893 56. Taylor A, Rothstein D, Rudd CE. Small-molecule inhibition of PD-1 transcription Is
894 an effective alternative to antibody blockade in cancer therapy. Cancer Res.
895 2018;78(3):706-17.
896 57. Krueger J, Rudd CE. Two Strings in One Bow: PD-1 Negatively Regulates via Co-
897 receptor CD28 on T Cells. Immunity. 2017;46(4):529-31.
898 58. Steele L, Mannion AJ, Shaw G, Maclennan KA, Cook GP, Rudd CE, et al. Non-
899 redundant activity of GSK-3alpha and GSK-3beta in T cell-mediated tumor rejection.
900 iScience. 2021;24(6):102555.
901 59. Taylor A, Rudd CE. Glycogen Synthase Kinase 3 Inactivation Compensates for the
902 Lack of CD28 in the Priming of CD8(+) Cytotoxic T-Cells: Implications for anti-PD-1
903 Immunotherapy. Front Immunol. 2017;8:1653.
904 60. Huntington KE, Louie AD, Srinivasan PR, Schorl C, Lu S, Silverberg D, et al. GSK-3
905 Inhibitor Elraglusib Enhances Tumor-Infiltrating Immune Cell Activation in Tumor Biopsies
906 and Synergizes with Anti-PD-L1 in a Murine Model of Colorectal Cancer. Int J Mol Sci.
907 2023;24(13).
908 61. Shaw G, Cavalcante L, Giles FJ, Taylor A. Elraglusib (9-ING-41), a selective small-
909 molecule inhibitor of glycogen synthase kinase-3 beta, reduces expression of immune
910 checkpoint molecules PD-1, TIGIT and LAG-3 and enhances CD8(+) T cell cytolytic killing
911 of melanoma cells. J Hematol Oncol. 2022;15(1):134.
912 62. Van Oers NS, Garvin AM, Davis CB, Forbush KA, Carlow DA, Littman DR, et al.
913 Disruption of CD8-dependent negative and positive selection of thymocytes is correlated

914 with a decreased association between CD8 and the protein tyrosine kinase, p56lck. Eur J
915 Immunol. 1992;22(3):735-43.
916 63. Barber DL, Wherry EJ, Masopust D, Zhu B, Allison JP, Sharpe AH, et al. Restoring
917 function in exhausted CD8 T cells during chronic viral infection. Nature.
918 2006;439(7077):682-7.
919 64. Kim HD, Jeong S, Park S, Lee YJ, Ju YS, Kim D, et al. Implication of CD69(+)
920 CD103(+) tissue-resident-like CD8(+) T cells as a potential immunotherapeutic target for
921 cholangiocarcinoma. Liver Int. 2021;41(4):764-76.
922 65. Wherry EJ. T cell exhaustion. Nature immunology. 2011;12(6):492-9.
923 66. Abadie K, Clark EC, Valanparambil RM, Ukogu O, Yang W, Daza RM, et al.
924 Reversible, tunable epigenetic silencing of TCF1 generates flexibility in the T cell memory
925 decision. Immunity. 2024;57(2):271-86 e13.
926 67. Ke Xu NY, Min Peng, Efstathios G. Stamatiades, Amy Shyu1,4, Peng Li1, Xian
927 Zhang1, Mytrang H. Do1,2, Zhaoquan Wang1,2, Kristelle J. Capistrano1, Chun Chou1,
928 Andrew G. Levine1,2, Alexander Y. Rudensky1,2,5, Ming O. Li1,2†. Glycolysis fuels
929 phosphoinositide 3-kinase signaling to bolster T cell immunity. Science. 2021.
930 68. Wu M, Fu X, Xu R, Liu S, Li R, Xu J, et al. Glucose metabolism and function of
931 CD4(+) Tregs are regulated by the TLR8/mTOR signal in an environment of SKOV3 cell
932 growth. Cancer Med. 2023;12(15):16310-22.
933 69. Sicheng Fu1 SZ, Chenxi Tian, Shiyu Bai1, Jiqian Zhang, Chonglun Zhan, Di Xie, Lu
934 Wang, Zonghong Li. Immunometabolism regulates TCR recycling and iNKT cell functions.
935 Scisignal. 2019.
936 70. Palmer CS, Hussain T, Duette G, Weller TJ, Ostrowski M, Sada-Ovalle I, et al.
937 Regulators of Glucose Metabolism in CD4(+) and CD8(+) T Cells. Int Rev Immunol.
938 2016;35(6):477-88.
939 71. Frauwirth KA, Riley JL, Harris MH, Parry RV, Rathmell JC, Plas DR, et al. The CD28
940 signaling pathway regulates glucose metabolism. Immunity. 2002;16(6):769-77.
941 72. Macintyre AN, Gerriets VA, Nichols AG, Michalek RD, Rudolph MC, Deoliveira D, et
942 al. The glucose transporter Glut1 is selectively essential for CD4 T cell activation and
943 effector function. Cell Metab. 2014;20(1):61-72.
944 73. Gantt KR, Cherry J, Richardson M, Karschner V, Atasoy U, Pekala PH. The
945 regulation of glucose transporter (GLUT1) expression by the RNA binding protein HuR. J
946 Cell Biochem. 2006;99(2):565-74.

947 74. Sakaguchi S, Yamaguchi T, Nomura T, Ono M. Regulatory T cells and immune
948 tolerance. Cell. 2008;133(5):775-87.
949 75. Allard D, Chrobak P, Allard B, Messaoudi N, Stagg J. Targeting the CD73-adenosine
950 axis in immuno-oncology. Immunol Lett. 2019;205:31-9.
951 76. Gomez-Rodriguez J, Kraus ZJ, Schwartzberg PL. Tec family kinases Itk and Rlk /
952 Txk in T lymphocytes: cross-regulation of cytokine production and T-cell fates. FEBS J.
953 2011;278(12):1980-9.
954 77. Das A, Martinez-Ruiz GU, Bouladoux N, Stacy A, Moraly J, Vega-Sendino M, et al.
955 Transcription factor Tox2 is required for metabolic adaptation and tissue residency of ILC3
956 in the gut. Immunity. 2024;57(5):1019-36 e9.
957 78. Russell JH, Ley TJ. Lymphocyte-mediated cytotoxicity. Annu Rev Immunol.
958 2002;20:323-70.
959 79. Osinska I, Popko K, Demkow U. Perforin: an important player in immune response.
960 Cent Eur J Immunol. 2014;39(1):109-15.
961 80. Kurschus FC, Jenne DE. Delivery and therapeutic potential of human granzyme B.
962 Immunol Rev. 2010;235(1):159-71.
963 81. Vick SC, Kolupaev OV, Perou CM, Serody JS. Anti-PD-1 Checkpoint Therapy Can
964 Promote the Function and Survival of Regulatory T Cells. J Immunol. 2021;207(10):2598-
965 607.
966 82. Kamada T, Togashi Y, Tay C, Ha D, Sasaki A, Nakamura Y, et al. PD-1(+)
967 regulatory T cells amplified by PD-1 blockade promote hyperprogression of cancer. Proc
968 Natl Acad Sci U S A. 2019;116(20):9999-10008.
969 83. Woods DM, Ramakrishnan R, Laino AS, Berglund A, Walton K, Betts BC, et al.
970 Decreased Suppression and Increased Phosphorylated STAT3 in Regulatory T Cells are
971 Associated with Benefit from Adjuvant PD-1 Blockade in Resected Metastatic Melanoma.
972 Clin Cancer Res. 2018;24(24):6236-47.
973 84. Dodagatta-Marri E, Meyer DS, Reeves MQ, Paniagua R, To MD, Binnewies M, et al.
974 alpha-PD-1 therapy elevates Treg/Th balance and increases tumor cell pSmad3 that are
975 both targeted by alpha-TGFbeta antibody to promote durable rejection and immunity in
976 squamous cell carcinomas. J Immunother Cancer. 2019;7(1):62.
977 85. Banerjee H, Nieves-Rosado H, Kulkarni A, Murter B, McGrath KV, Chandran UR, et
978 al. Expression of Tim-3 drives phenotypic and functional changes in Treg cells in secondary
979 lymphoid organs and the tumor microenvironment. Cell Rep. 2021;36(11):109699.

980 86. Arce Vargas F, Furness AJS, Litchfield K, Joshi K, Rosenthal R, Ghorani E, et al. Fc
981 Effector Function Contributes to the Activity of Human Anti-CTLA-4 Antibodies. Cancer Cell.
982 2018;33(4):649-63 e4.
983 87. Joshi NS, Cui W, Chandele A, Lee HK, Urso DR, Hagman J, et al. Inflammation
984 directs memory precursor and short-lived effector CD8(+) T cell fates via the graded
985 expression of T-bet transcription factor. Immunity. 2007;27(2):281-95.
986 88. Plumlee CR, Obar JJ, Colpitts SL, Jellison ER, Haining WN, Lefrancois L, et al. Early
987 Effector CD8 T Cells Display Plasticity in Populating the Short-Lived Effector and Memory-
988 Precursor Pools Following Bacterial or Viral Infection. Sci Rep. 2015;5:12264.
989 89. Ye Z, Gould TM, Zhang H, Jin J, Weyand CM, Goronzy JJ. The GSK3beta-beta-
990 catenin-TCF1 pathway improves naive T cell activation in old adults by upregulating miR-
991 181a. NPJ Aging Mech Dis. 2021;7(1):4.
992 90. Fu Y, Wang J, Liu C, Liao K, Gao X, Tang R, et al. Glycogen synthase kinase 3
993 controls T-cell exhaustion by regulating NFAT activation. Cell Mol Immunol.
994 2023;20(10):1127-39.
995 91. Utzschneider DT, Charmoy M, Chennupati V, Pousse L, Ferreira DP, Calderon-
996 Copete S, et al. T Cell Factor 1-Expressing Memory-like CD8(+) T Cells Sustain the
997 Immune Response to Chronic Viral Infections. Immunity. 2016;45(2):415-27.
998 92. Im SJ, Hashimoto M, Gerner MY, Lee J, Kissick HT, Burger MC, et al. Defining
999 CD8+ T cells that provide the proliferative burst after PD-1 therapy. Nature.
1000 2016;537(7620):417-21.
1001 93. Ivanova ME, Lukoyanova N, Malhotra S, Topf M, Trapani JA, Voskoboinik I, et al.
1002 The pore conformation of lymphocyte perforin. Sci Adv. 2022;8(6):eabk3147.
1003 94. Buck MD, Sowell RT, Kaech SM, Pearce EL. Metabolic Instruction of Immunity. Cell.
1004 2017;169(4):570-86.
1005 95. O'Sullivan D, Pearce EL. Targeting T cell metabolism for therapy. Trends Immunol.
1006 2015;36(2):71-80.
1007 96. Pearce EL, Poffenberger MC, Chang CH, Jones RG. Fueling immunity: insights into
1008 metabolism and lymphocyte function. Science. 2013;342(6155):1242454.
1009 97. Jellusova J, Cato MH, Apgar JR, Ramezani-Rad P, Leung CR, Chen C, et al. Gsk3
1010 is a metabolic checkpoint regulator in B cells. Nat Immunol. 2017;18(3):303-12.

1011 98. Kim A, Lopez S, Smith S, Sony A, Abreu J, de la Parra C, et al. Interleukin 24
1012 Promotes Mitochondrial Dysfunction, Glucose Regulation, and Apoptosis by Inactivating
1013 Glycogen Synthase Kinase 3 Beta in Human Prostate Cancer Cells. Cells. 2025;14(5).
1014 99. Moes B, Rudd CE. Comment on: Glycogen synthase kinase 3 controls T-cell
1015 exhaustion by regulating NFAT activation. Cell Mol Immunol. 2025.
1016 100. Welsh RM, Seedhom MO. Lymphocytic choriomeningitis virus (LCMV): propagation,
1017 quantitation, and storage. Curr Protoc Microbiol. 2008;Chapter 15:Unit 15A 1.
1018 101. Raab M, da Silva AJ, Findell PR, Rudd CE. Regulation of Vav-SLP-76 binding by
1019 ZAP-70 and its relevance to TCR zeta/CD3 induction of interleukin-2. Immunity.
1020 1997;6(2):155-64.
1021 102. Helft J, Bottcher J, Chakravarty P, Zelenay S, Huotari J, Schraml BU, et al. GM-CSF
1022 Mouse Bone Marrow Cultures Comprise a Heterogeneous Population of CD11c(+)MHCII(+)
1023 Macrophages and Dendritic Cells. Immunity. 2015;42(6):1197-211.

1024

1025

1026 **Figure Legends:**
1027

1028 **Fig. 1: GSK-3 KD regulates T-cell progenitors and exhaustion.** (**A**) Western blot analysis
1029 of GSK-3 expression in splenic T cells (n=3) Characterization of CD8+ T cell responses
1030 following LCMV infection. Mice were infected with LCMV clone 13 (cl13) or Armstrong strain,
1031 and spleens were harvested at day 30 or day 7 post-infection (p.i.), respectively. (**B-C**)
1032 Weight loss following infection with (**B**) LCMV-cl13 (n=14, pooled from 3 independent
1033 experiments) or (**C**) LCMV Armstrong (n=5, representative of 2 independent experiments).
1034 (**D**) Splenic CD8+ T cell counts in naive and LCMV-infected mice (Armstrong d7 p.i. and CL-
1035 13 d30 p.i.; n=6-14, pooled from ≥2 independent experiments). (**E**) Flow cytometry analysis
1036 and quantification of GP33+ CD8+ effector memory (TEM: CD62L-CD44+) and central
1037 memory (TCM: CD44+CD62L+) T cells (n=6-8, pooled from 2 independent experiments). (**F**)
1038 Quantification of GP33+ CD8+ terminal effector (KLRG1+CD39+) cells (n=6, pooled from 2
1039 independent experiments). (**G**) Proportion of TEM and TCM among GP33+ CD8+ T cells
1040 after LCMV Armstrong infection (n=5-6, pooled from 2 independent experiments). (**H**) The
1041 precent TCF-1 expression in naive, activated GP33+, TCM, and TEM CD8+ T cells (n=5-7,
1042 representative of 2 independent experiments). (**I-J**) Flow cytometry profile (**I**) and histogram
1043 quantification (**J**) of short-lived effector cells (SLEC: KLRG1+CD127-) and memory precursor
1044 effector cells (MPEC: KLRG1-CD127+) among GP33+ CD8+ T cells (n=7-12, pooled from 2
1045 independent experiments). (**K-L**) Percent TCF-1 expression (**K**) and representative plots (**L**)
1046 in SLEC and MPEC populations (n=7-12, pooled from 2 independent experiments). (**M**)
1047 Histogram showing Ki67 expression in SLEC and MPEC populations (n=6-7). Upper panel:
1048 GP33+MPEC+; lower panel: GP33+SLEC+ (**N**) Expression of exhaustion markers PD1,
1049 TIM3, and CD101 on GP33+ CD8+ T cells (n=12-14, pooled from 2 independent
1050 experiments). (**O**) Distribution of stem-like (TIM3-TCF1+), transitory (CX3CR1+TIM3+CD101-
1051), and terminal exhausted (CX3CR1-TIM3+CD101+) cells among PD1+GP33+ CD8+ T cells
1052 (n=12-14, pooled from ≥2 independent experiments). (**P**) Ki67 expression in stem-like,
1053 transitory, and terminal exhausted populations (n=7-8). Data presented as mean ± SEM.
1054 Statistical significance determined by unpaired t-test: *p<0.05, **p<0.01, ***p<0.001,
1055 ****p<0.0001; NS, not significant.
1056

1057 **Fig. 2: Metabolic profiling of T cells from WT and dLCK-CRE mice.**(**A**) Representative
1058 flow cytometry plots of Tag-it staining in splenic CD8+ T cells stimulated with varying

1059 concentrations of anti-CD3ε monoclonal antibodies (mAbs) for 48 hours. (**B**) Proportion of
1060 KI67+ cells among CD8+ T cells, with blue arrow indicating lowest anti-CD3ε mAb
1061 concentration tested (n=6, pooled from 2 independent experiments). (**C**) Extracellular
1062 acidification rate (ECAR) in splenic T cells following 24h activation with anti-CD3ε (1μg/mL).
1063 Sequential injections: glucose, oligomycin, and 2-DG. (**D-F**) Quantification of glycolytic
1064 parameters: glycolysis (**D**), glycolytic capacity (**E**), and glycolytic reserve (**F**) (n=3). (**G**)
1065 Oxygen consumption rate (OCR) in T cells activated with anti-CD3ε (1μg/mL) for 24h.
1066 Sequential injections: oligomycin, FCCP, and rotenone/antimycin A (Rot/AA). (**G-K**)
1067 Quantification of respiratory parameters: basal respiration, maximal respiration, spare
1068 capacity, and ATP production (n=3). (**L**) Ratio of maximal OCR to maximal ECAR. (**M-N**)
1069 Glucose uptake measured by NDBG mean fluorescence intensity (MFI) in CD8+ and CD4+
1070 T-cells, unstimulated (NS) or activated with anti-CD3ε (1μg/mL) for 24h (n=5-6). (**O-P**) GLUT-
1071 1 expression analysis by flow cytometry in CD8+ and CD4+ T cells, unstimulated (NS) or
1072 activated with anti-CD3ε (1μg/mL) for 24h (n=5-6). Data represent mean ± SEM from 2-3
1073 independent experiments. (**Q-R**) GLUT-1, CD44 and GZMB MFI expression analysis by flow
1074 cytometry in GP33+CD8+ MPEC+ (O) and GP33+CD8+ SLEC+ T cells (P) from LCMVCl13
1075 infected mice (see Figure 2). Statistical analysis: unpaired t-test (*p<0.05, **p<0.01,
1076 ***p<0.001, ****p<0.0001; NS, not significant).
1077
1078 **Fig. 3: CyTOF and flow cytometric analysis of subsets of TILs induced by GSK-3 SMI**
1079 **enabling of anti-PD-1 therapy to resist tumor growth.** (**A**) Schematic of experimental
1080 design. (**B,C**) Tumor volume quantification at day 16 post-implementation under indicated
1081 conditions (n=5-10, data pooled from ≥2 independent experiments). GSK-3i licenses anti-PD-
1082 1 to control the growth of the B16 F10 R1 tumor, otherwise resistant to monotherapy. (**D**) Left
1083 panels: Representative spider plots showing tumor progression; Right panel: Circular plots
1084 depicting proportions of responders versus non-responders following B16F10 implantation
1085 and anti-PD1 treatment with (orange) or without GSK-3 SMI (blue) (data pooled from 4
1086 independent experiments). (**E**) Phenograph visualization of tumor-infiltrating immune cell
1087 populations by CyTOF analysis (n=5-10). (**F**) Representative heatmap showing key subsets
1088 of TILs altered by mono and combination therapy. (**G**) boxplots showing distribution of
1089 immune cell subsets identified by CyTOF. (**H**) Quantification of the percent frequency of
1090 CD8+ effector (EFF) TILs and (**I**) their lack of an effect on tumor mass. (**J**) Quantification of
1091 the percent frequency of CD8+ effector memory (EM) T cells among TILs and (**K**) the

1092 correlation analysis between CD8+ TEM TIL frequency and tumor mass (n=3). (**L)**
1093 Quantification of total CD4+ T cells and (**M)** regulatory T cells (CD25+FOXP3+CD25+),
1094 respectively (n=3).
1095
1096 **Fig. 4: Transcriptome profiling of gene expression in TILs in response to GSK-3-anti-**
1097 **PD1 cooperation in cancer therapy** Analysis of differentially expressed genes in CD8+
1098 tumor-infiltrating lymphocytes (TILs). (**A**) Venn diagram of differentially expressed genes in
1099 CD8+ TILs after RNA sequencing. (**B-C**) Representative volcano plots from RNA
1100 sequencing. Genes with a log2-fold change in expression greater highlighted in red. (**D**)
1101 Representative heatmap of overexpressed genes with a log2-fold change in expression
1102 greater than 1 and a p-value of 0.001. (**E-F**) Representative heatmap of cytotoxic genes with
1103 a log2-fold change in expression greater than 1. (**G**) Quantification of the proportion of dead
1104 cells following a killing assay with GZMD and F siRNA knockdown. (**H**) Quantification
1105 of *tcf7* mRNA levels (reads per million, RPM) in CD8+ TILs. Data are shown as mean ± SEM.
1106 Statistical significance was determined by unpaired t-test (*p < 0.05, **p < 0.01, ***p < 0.001,
1107 ****p < 0.0001, NS: not significant). n = 3 with 4-5 mice per group in each experiment.
1108
1109 **Fig. 5: GSK-3 KD licences anti-PD-1 blockade to generate super-armed CD8+ CTL TILs**
1110 **in tumors.** B16F10 implanted WT and dLCK-CRE mice were injected or not with anti-PD1.
1111 (**A**) Tumor volume in control (ctrl) and dLck-Cre mice with or without anti-PD-1 treatment. (**B**)
1112 Tumor weight 16 days post-implantation. (**C**) Representative flow cytometry plots of CD4 and
1113 CD8+ TILs following checkpoint blockade in WT and dLck Cre mice. (**D**) Numbers of CD8+
1114 TILs per gram of tumor tissue. **(E**) Expression and proportion of perforin, granzyme A, B, C,
1115 and F in CD44+CD8+ TILs in WT and dLck Cre mice. Data are presented as mean ± SEM.
1116 Statistical significance was determined by unpaired t-test (*p < 0.05, **p < 0.01, ***p < 0.001,
1117 ****p < 0.0001, NS: not significant). n = 3 experiments with 4--5 mice per group**.**
1118
1119 **Fig. 6: GSK-3 regulates CD4+-CD8 cooperation needed for the efficacy of PD-1**
1120 **blockade to generation multi-granzyme CTLs in tumors.** (**A**) Quantification of CD4+
1121 tumor-infiltrating lymphocytes (TILs) in wild-type (WT) and dLCK-Cre mice with or without
1122 anti-PD-1 treatment. (**B**) Representative flow cytometry analysis of CD4+ Treg and helper
1123 TILs in WT and dLck-Cre mice following anti-PD-1 therapy. (**C-E**) Representative flow
1124 cytometry plots (**C**) and histogram quantification **(D, E**) of TIM3+ expression on CD44+CD4+

1125 TILs with or without anti-PD-1 treatment. (**F, G**) Measurement of tumor volume (**F**) and weight
1126 (**G**) following CD4+ T cell depletion. (**H**) Representative flow cytometry plots of the presence
1127 of CD8+ TILs after CD4+ T cell depletion. (**I**) Measure of the numbers of CD8+ TILs/g of
1128 tumor after CD4+ T cell depletion. (**J**) Quantification of the loss of the induced expression of
1129 perforin, granzyme A, B, C, and F expression in CD44+CD8+ TILs after CD4+ T cell
1130 depletion in GSK-3 KD mice, shown as mean fluorescence intensity (MFI) (upper panel) and
1131 percentage (lower panel). Quantification of target cell killing with or without anti-PD-1
1132 treatment. (**K**) Depletion of Tregs with anti-CTLA-4 reversed the inhibition of tumor regression
1133 in WT mice while not affecting the ability of dLck-Cre mice to limit tumor growth. Data are
1134 presented as mean ± SEM. Statistical significance was determined by unpaired t-test (*$p < 0.05$, **$p < 0.01$, ***$p < 0.001$, ****$p < 0.0001$, NS: not significant). n = 4-5 mice per group.

1136

1137

Figure 1

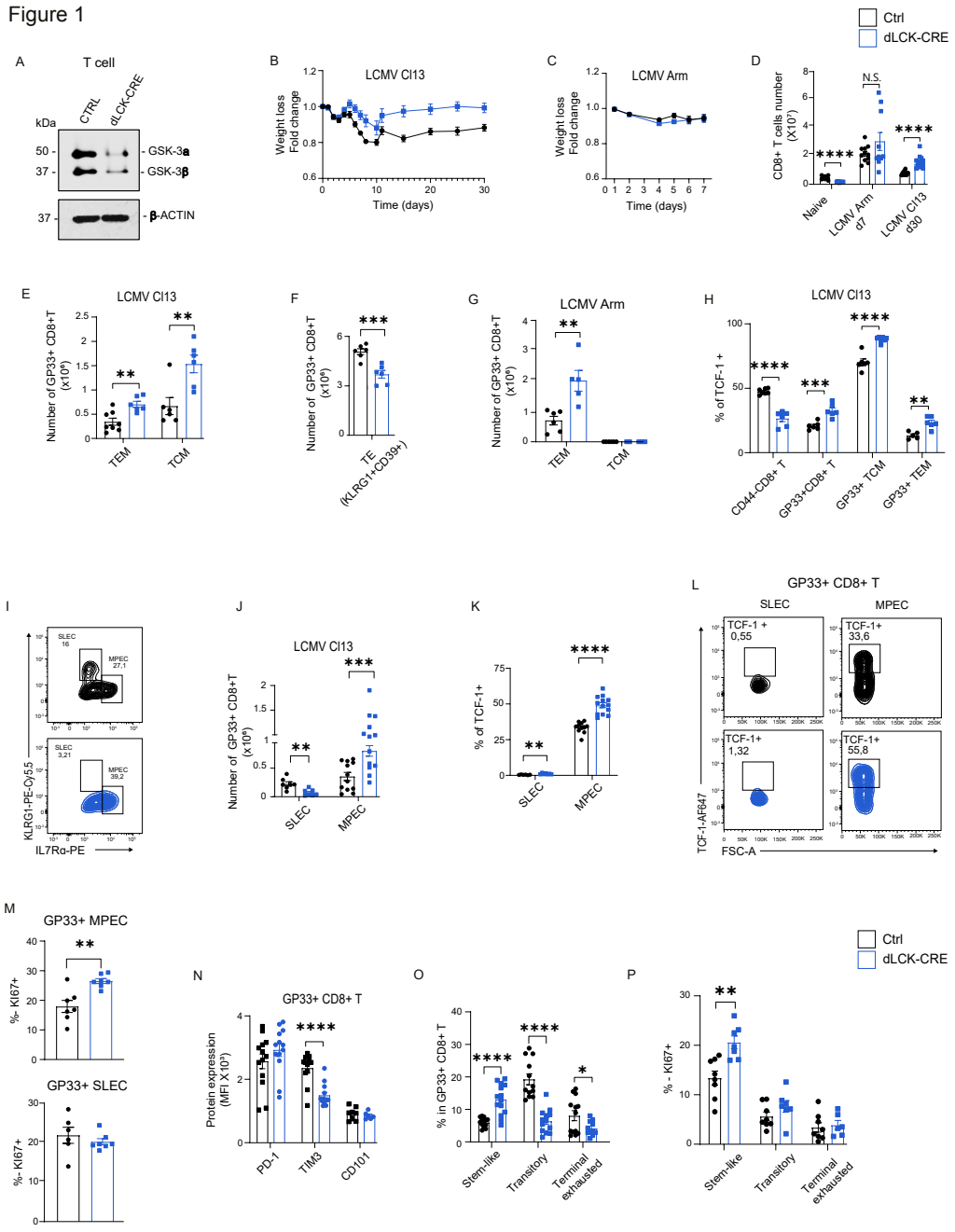

1138

Figure 2

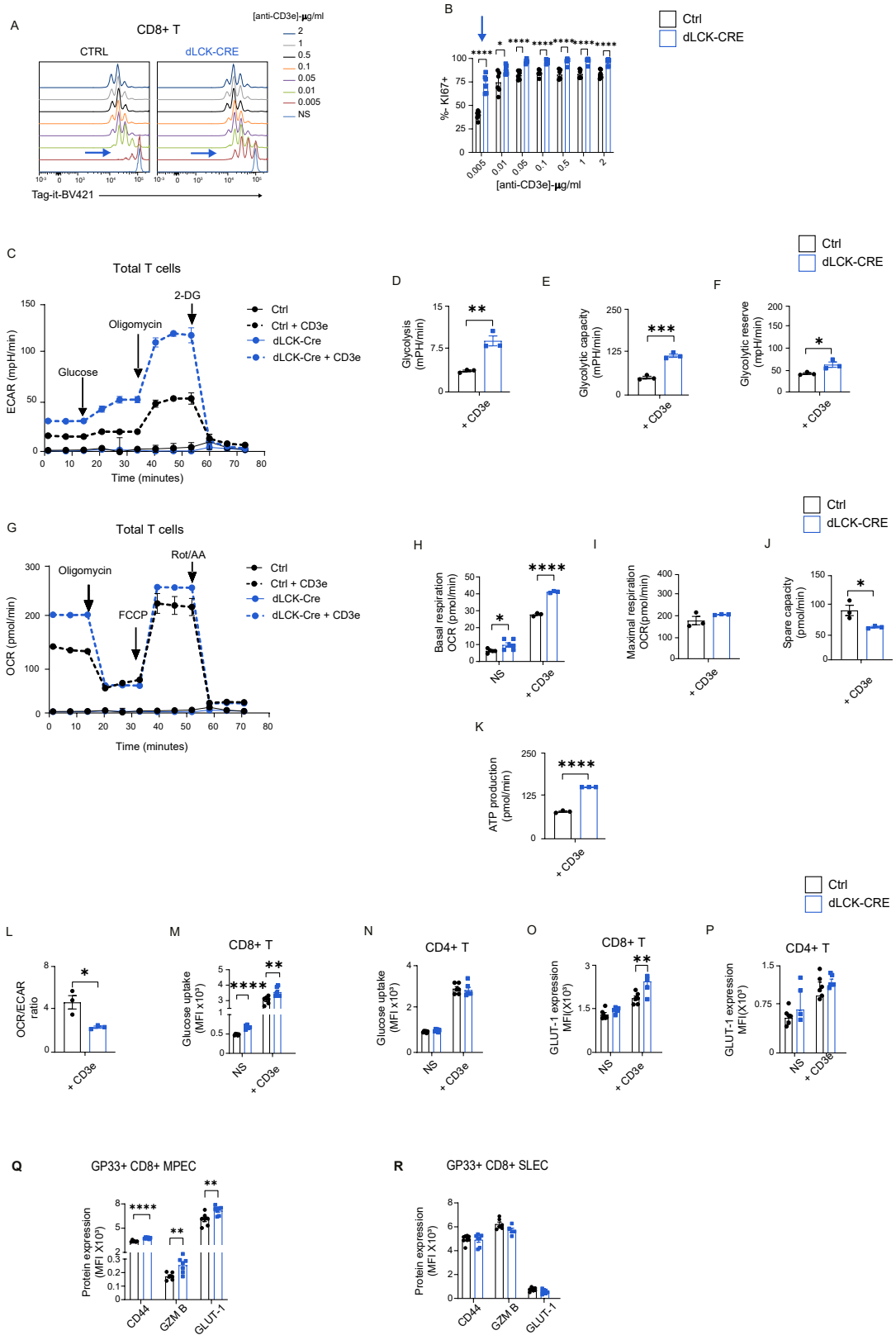

1139

1140

Figure 3

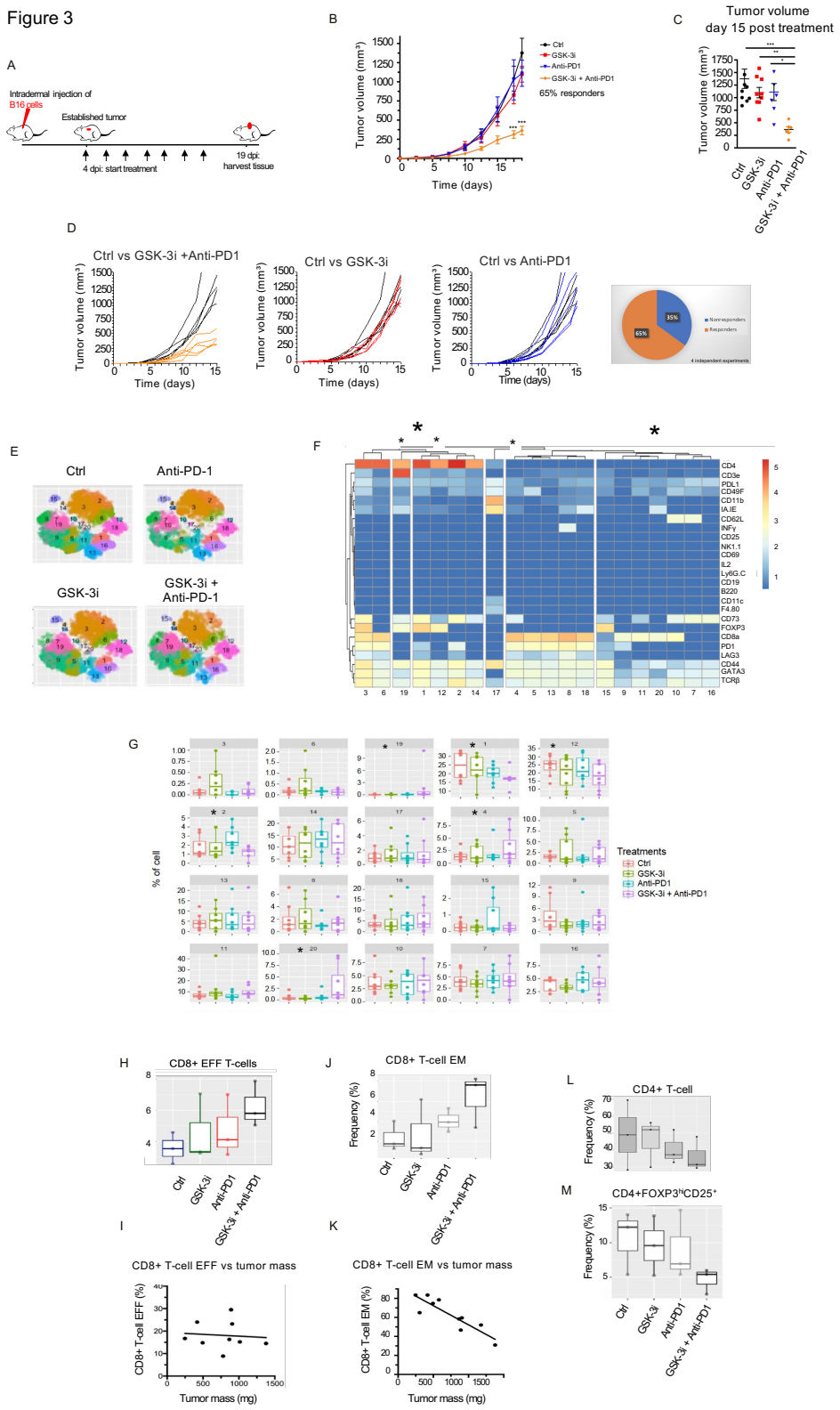

1141

Figure 4

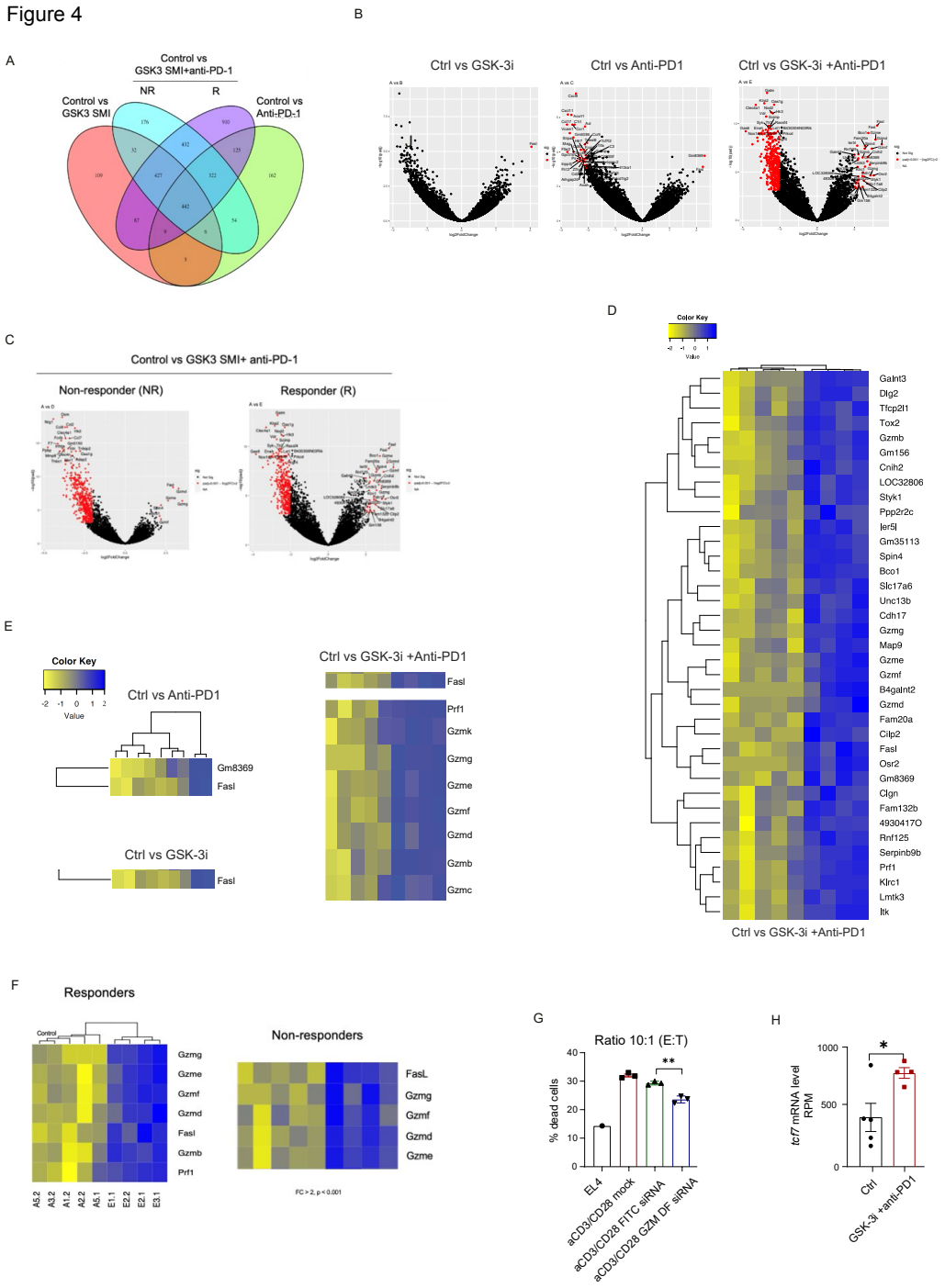

1142

Figure 5

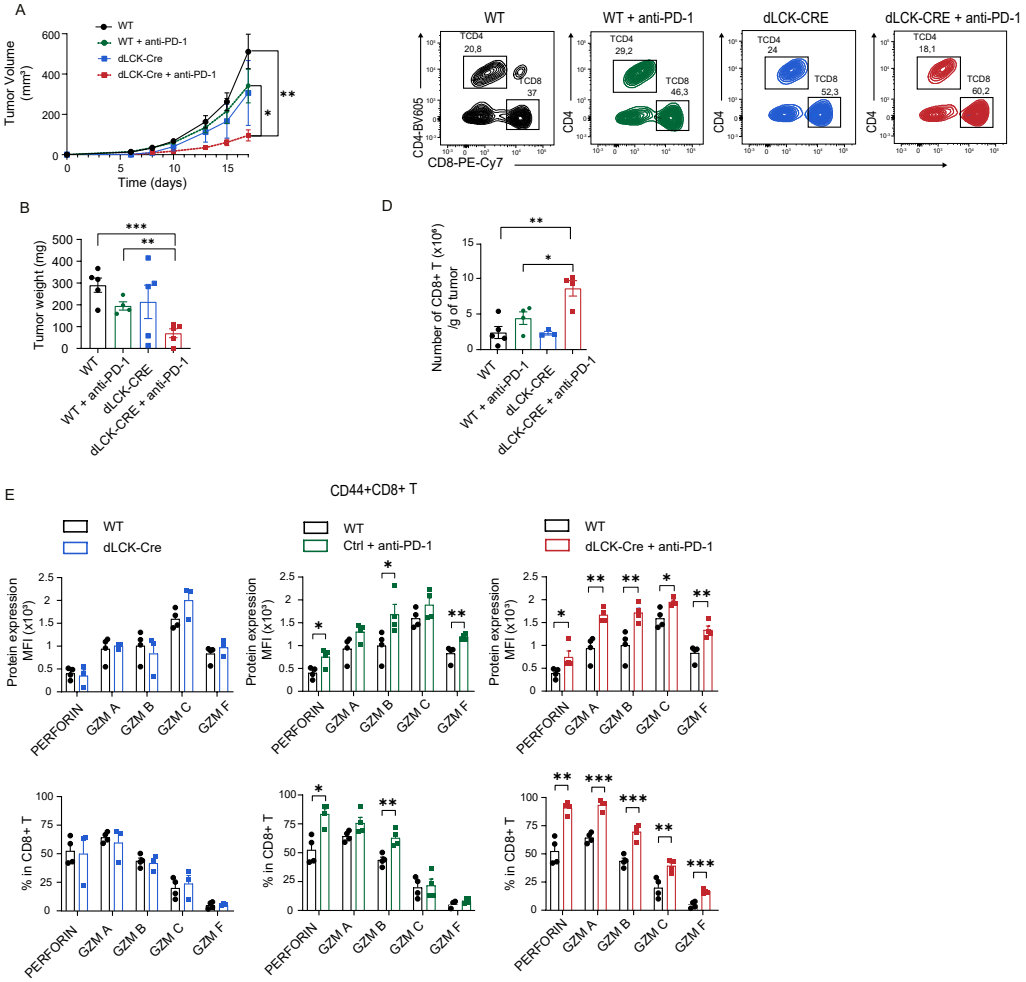

1143

1144

Figure 6

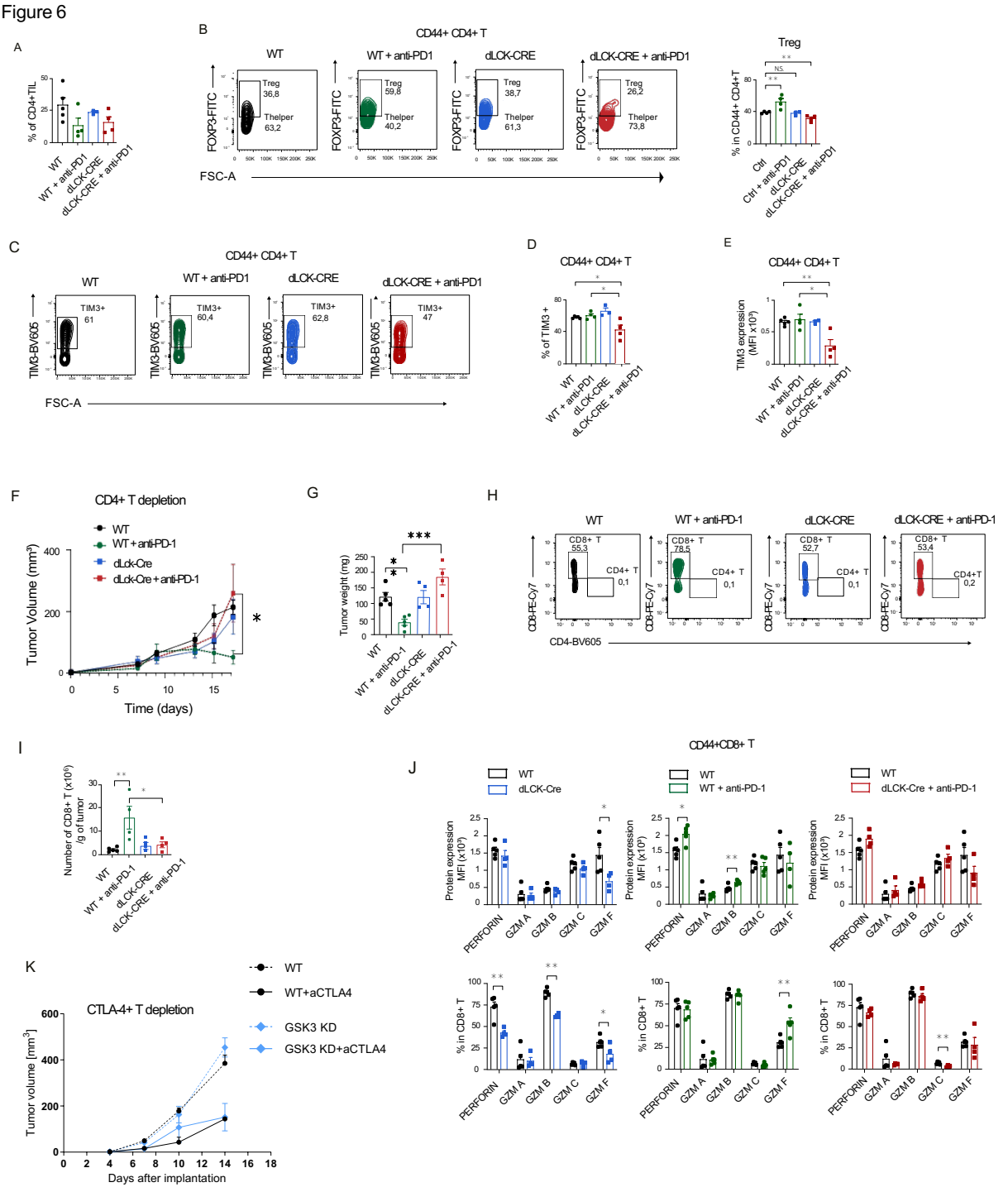

1145

Supplementary Figure S1

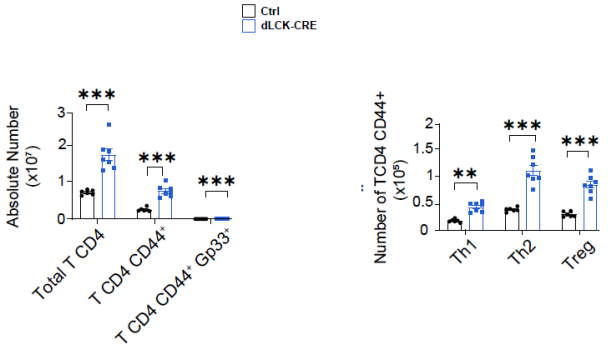

Fig. S1: Flow cytometric characterization of splenic CD4+ T cell subsets in dLckCre (GSK-3KD) mice 30 days post-LCMV Cl13 infection. Left: Elevated numbers of total CD4 + T cells, CD44+CD4+ T cells, and CD44+Gp33+CD4+ T cells in GSK-3KD mice relative to controls. Right: Increased frequencies of Th1, Th2, and regulatory T cell populations in GSK-3KD mice. Analysis performed using anti-TCR beta, CD4, CD8, and FoxP3 antibodies.

1146

Supplementary Figure S2

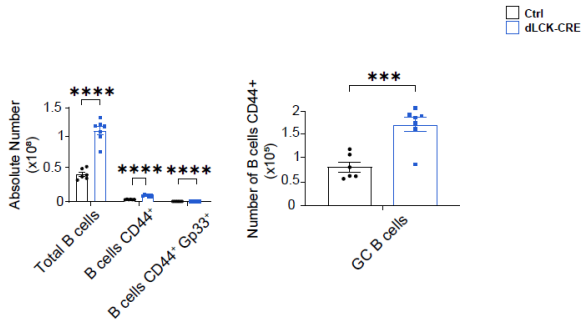

Fig. S2: Flow cytometric analysis of splenic B cell populations in dLckCre (GSK-3KD) mice 30 days post- LCMV Cl13 infection. Left panel: Quantification of total B cells, CD44+ B cells, and CD44+Gp33+ B cells shows significant expansion in GSK-3KD mice compared to controls. Right panel: Enhanced germinal center CD44+ B cell numbers in GSK-3KD mice. Cell populations were identified using anti-CD19, CD44, and Gp33 tetramer staining.

1147

1148

1149

Supplementary Figure S3

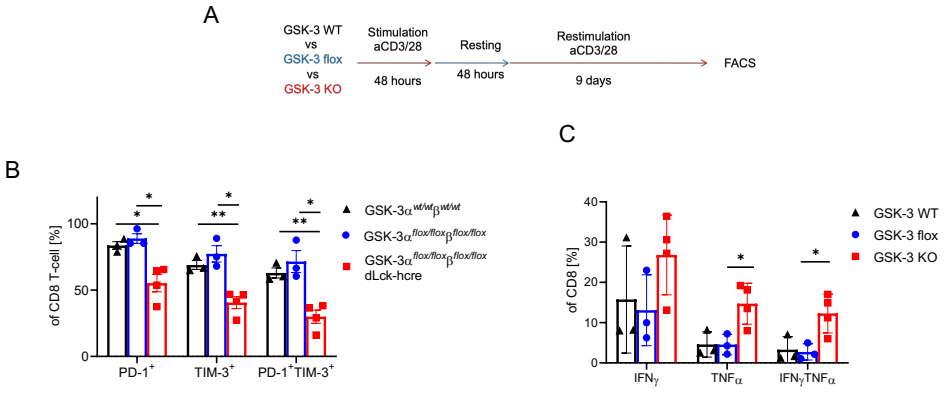

Fig. S3: Knockout of GSK-3 in CD8 T cells confers resistance to *in vitro* exhaustion and enhances IFN-γ and TNF-α production. Splenic T cells were activated and restimulated according to the protocol outlined in Panel A. This process resulted in the upregulated expression of the exhaustion markers PD-1 and TIM-3 in both wild-type (WT) and floxed control T cells. Conversely, T cells deficient in GSK-3 (GSK-3-/- Lck Cre T cells) displayed significantly reduced levels of PD-1 and TIM-3 expression (B). Notably, the frequency of cells co-producing IFN-γ and TNF-α increased in GSK-3 Lck Cre T cells (C).

1150

Supplementary Figure S4

	Control	PD1	SB	PD1_SB
20	0.468	0.818	0.867	0.013
1	0.000	0.596	0.207	0.044
19	0.940	0.962	0.963	0.099
12	0.000	0.312	0.714	0.127
4	0.065	0.765	0.704	0.149
9	0.000	0.092	0.310	0.237
2	0.000	0.881	0.106	0.338
18	0.089	0.635	0.422	0.404
11	0.009	0.185	0.785	0.431
17	0.065	0.490	0.658	0.458
16	0.000	0.581	0.440	0.511
14	0.000	0.956	0.540	0.589
13	0.041	0.639	0.534	0.619
8	0.009	0.792	0.401	0.683
6	0.141	0.104	0.821	0.691
15	0.143	0.842	0.077	0.763
7	0.000	0.498	0.991	0.767
5	0.086	0.391	0.762	0.828
3	0.222	0.046	0.554	0.965
10	0.000	0.497	0.712	0.981

Fig. S3: Statistical evaluation of mass cytometry (CyTOF) data comparing tumor-infiltrating lymphocyte subsets across treatment groups (control, anti-PD-1 monotherapy, SB415286 monotherapy, and combined anti-PD- 1/SB415286). Clusters 20 and 1 showed statistically significant differences ($p<0.05$) for combination therapy relative to other treatment groups. Analysis based on three independent experiments with four mice per treatment group (n=3, 4 mice/group).

1151

Supplementary Figure S5

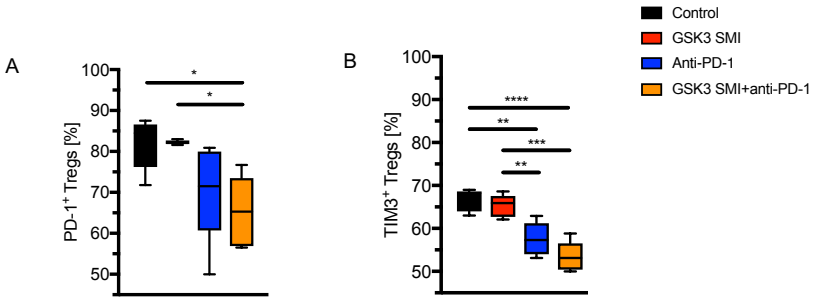

Fig S5: Flow cytometric validation showing the decrease in CD4+FoxP3+ TILs with reduced PD-1 and TIM3 expression in response to anti-PD1/GSK3i therapy. TILs were extracted from B16-F10 R1 tumors and stained for CD4, FoxP3, CD25, PD-1, TIM3, LAG3 and PDL-1 and assessed for expression. (A) Percentage of PD-1+ cells within the Treg population decreases with combination therapy. (B) Percentage of TIM3+ cells within the Treg population decreases with combination therapy.

Supplementary Figure S6

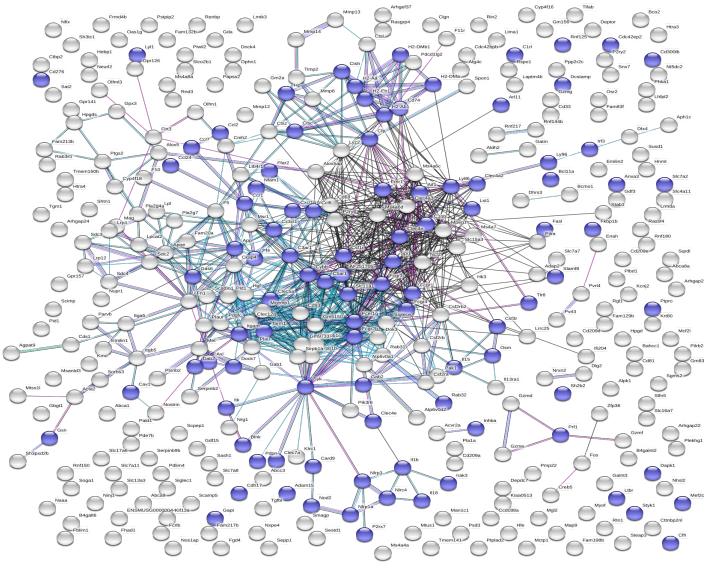

Figure S6:
Gene regulatory network illustrating the synergistic upregulation of immunomodulatory gene signatures induced by combination treatment with anti-PD-1 and GSK-3 inhibition (see blue), as evidenced by the enrichment of genes associated with immune activation and inflammatory response pathways (shown as central network).

1156

1157

Supplemental Data Figure S7

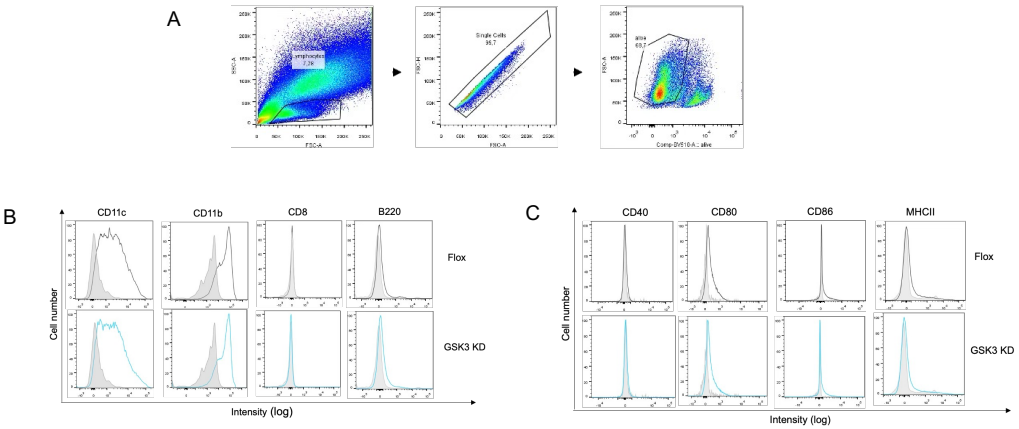

Fig: S7 The phenotype of GM-CSF treated bone marrow dendritic cells from GSK-3KD and WT mice are the same. Bone marrow cells were isolated and cultured in medium containing GM-CSF (granulocyte-macrophage colony-stimulating factor), which stimulates the differentiation of hematopoietic progenitor cells into dendritic cells. Over the course of 6-8 days, the non-adherent cells are harvested and enriched for dendritic cells. (A) Gating strategy for DCs; (B) Flow cytometry panel showing equal expression of CD11c, CD11b and mutually low levels of CD8 and CD220. (C) Flow cytometry panel showing equal expression of CD80 and mutually low levels of MHC class II and CD86 .

1158